ARTICLES
https://doi.org/10.1038/s41558-021-01097-4

nature climate change

Observation-based early-warning signals for a collapse of the Atlantic Meridional Overturning Circulation

Niklas Boers[1,2,3] ✉

The Atlantic Meridional Overturning Circulation (AMOC), a major ocean current system transporting warm surface waters toward the northern Atlantic, has been suggested to exhibit two distinct modes of operation. A collapse from the currently attained strong to the weak mode would have severe impacts on the global climate system and further multi-stable Earth system components. Observations and recently suggested fingerprints of AMOC variability indicate a gradual weakening during the last decades, but estimates of the critical transition point remain uncertain. Here, a robust and general early-warning indicator for forthcoming critical transitions is introduced. Significant early-warning signals are found in eight independent AMOC indices, based on observational sea-surface temperature and salinity data from across the Atlantic Ocean basin. These results reveal spatially consistent empirical evidence that, in the course of the last century, the AMOC may have evolved from relatively stable conditions to a point close to a critical transition.

The Atlantic Meridional Overturning Circulation (AMOC) is the key circulation system of the Atlantic Ocean, transporting water masses northward at the surface and southward at the bottom of the ocean[1]. The AMOC is the archetypical example of potentially multi-stable Earth system components[2]. Early studies based on box models[3] indicated that the AMOC has two different stable states of operation, corresponding to a strong and a weak circulation mode. The AMOC's bistability and corresponding hysteresis were thereafter confirmed in a hierarchy of models, from Earth system models of intermediate complexity (EMICs)[4,5] to comprehensively coupled atmosphere–ocean general circulation models (AOGCMs)[6]. It should be noted, however, that AMOC bistability has not been identified in a considerable number of state-of-the-art Earth system models[7] (ESMs). It remains debated whether this should be interpreted as evidence for a monostable AMOC under current climate conditions, or rather as evidence for excessive AMOC stability in these models[8,9]: most comprehensive climate models probably underestimate the freshwater export from the northern Atlantic Ocean basin and hence suppress the associated destabilizing feedback[6,9–12]. Moreover, it has been argued that, in comprehensive models, very high spatial resolution is needed to obtain a good representation of the AMOC response to freshwater forcing[13]. Indeed, AMOC bistability has been revealed in recent simulations with a comprehensive model with an Eddy-permitting ocean module[14].

The strong AMOC state is currently attained, while the weak state has arguably been occupied recurringly during previous glacial intervals. Different lines of evidence from palaeoclimate proxy records indicate that Northern Hemisphere temperatures have varied abruptly at millennial time scales during previous glacial episodes, with corresponding changes of the AMOC between its weak and strong modes[1,15,16]. Speleothem and ocean sediment records from around the world show that these so-called Dansgaard–Oeschger (DO) cycles had (mainly because of the associated AMOC transitions) substantial impacts on global climate variability[17–19]. Complex interplays between the AMOC and North Atlantic sea-ice cover in conjunction with salinity and circulation changes have been proposed as physical causes underlying the DO cycles, but although the AMOC is widely accepted to play a key role, the exact chain of mechanisms is still under debate[16,20–22].

In EMICs and AOGCMs, a shift from the strong to the weak AMOC mode can be triggered by adding large amounts of freshwater to the North Atlantic, effectively reducing salinity there[14,23–26]. Such hosing experiments have been performed with a large number of AOGCMs; as noted above, hosing leads to AMOC shutdown in only a subset of models. Moreover, those models that exhibit AMOC shutdown disagree considerably regarding the exact amount of freshwater needed to trigger the shutdown[14,25,27,28], indicating that the sensitivity of the AMOC varies strongly across different models. The response of the AMOC to future CO_2 rise and associated warming has also been studied in different AOGCMs[27,29,30]. In addition to reducing salinity via enhanced meltwater inflow into the North Atlantic, thermal expansion due to overall rising global temperatures can also have the effect of decreasing AMOC strength. A collapse of the current AMOC state would have severe impacts on the global climate system[25,31] and would increase the risk of a cascade of further transitions in other major multi-stable components of the Earth system, such as the Antarctic ice sheet, tropical monsoon systems and Amazon rainforest[2,31].

Critical transitions between different equilibrium states of natural systems are preceded by characteristic properties of the fluctuations in the systems' dynamical behaviour that are referred to as critical slowing down[32–35]. For components of the Earth system that exhibit multiple stable equilibrium states[2], and in particular for the AMOC, indications of critical slowing down can provide key information for predicting future abrupt climate transitions, but also for climate change projections, climate model evaluation and the identification of adaptation and mitigation measures in general.

Critical slowing down is typically measured in terms of increasing variance and autocorrelation in time series encoding the

[1]Department of Mathematics and Computer Science, Freie Universität Berlin, Berlin, Germany. [2]Potsdam Institute of Climate Impact Research, Potsdam, Germany. [3]Department of Mathematics and Global Systems Institute, University of Exeter, Exeter, UK. ✉e-mail: boers@pik-potsdam.de

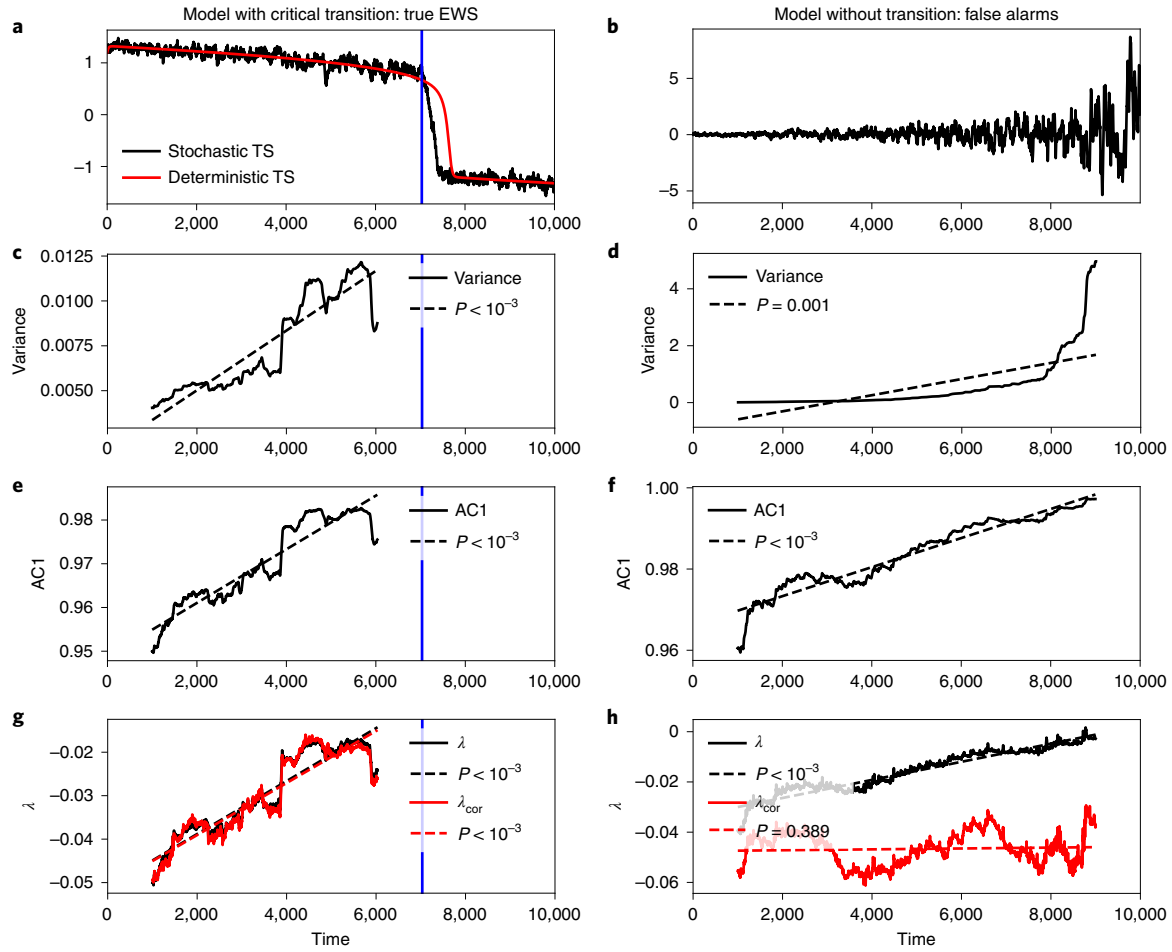

Fig. 1 | Comparison of robustness of different EWS indicators. a, Simulated time series from the non-linear model $dx/dt = -x^3 + x - T + \eta(t)$, with white noise $\eta(t)$ with standard deviation $\sigma = 0.2$, and control parameter T increasing linearly from $T = -1$ to $T = +1$. A critical transition occurs at around 7,000 model integration time steps (blue vertical line). A corresponding time series obtained by simulating the model without noise forcing, which represents the nonlinear trend that is used to detrend the stochastic time series, is shown in red for comparison. Note that the noise in the stochastic case causes the transition to occur earlier than in the deterministic case. **b**, Simulated time series from the linear model $dx/dt = -5x + \eta(t)$ with autocorrelated noise η, with the standard deviation σ of η rising linearly from 0.2 to 1.0 and the AR(1) coefficient of η rising linearly from 0.1 to 0.95. The system does hence not destabilize. Only the statistics of the noise forcing change. **c**, Variance of the time series shown in **a** with nonlinear trend removed. **d**, Variance of the time series shown in **b**. **e**, Lag-1 autocorrelation (AC1) of the time series shown in **a** with nonlinear trend removed. **f**, AC1 of the time series shown in **b**. **g**, The restoring rate λ of the time series shown in **a** with nonlinear trend removed, estimated under the assumption of Gaussian white noise (black) and assuming autocorrelated noise (red). **h**, The restoring rate λ of the time series shown in **b**, estimated under the assumption of Gaussian white noise (black) and assuming autocorrelated noise (red). Note that, for the model that undergoes a critical transition, all four indicators yield a significant warning (**c**,**e**,**g**). For the linear model with rising variance and AC1 of the noise term, the increases in variance, AC1 and the uncorrected λ give spurious EWS and hence false alarms, in contrast to the corrected restoring rate λ. All EWS indicators are estimated in sliding windows of size $w = 2{,}000$ time steps. The first and last $w/2 = 1{,}000$ time steps are omitted to ensure that each sliding window has the same number of data points (Methods). See Supplementary Fig. S1 for corresponding results using the nonlinear model forced with autocorrelated noise instead of white noise.

dynamics of the system under study[33,34,36]. These increases thus provide early-warning signals (EWS) for an abrupt transition to an alternative stable state, caused by a gradual change in the relevant control parameter. A potential problem with interpreting variance and autocorrelation increases as indicators for critical slowing down (and hence with using them as EWS for critical transitions) is that such increases can also be caused by increasing variance and autocorrelation of the external noise that forces the system. An additional indicator that is not biased in this way is therefore proposed here. The loss of stability when approaching a critical transition can be directly quantified in terms of the restoring rate[37] λ, obtained from linearization around a given stable equilibrium state x^*. For a system state x close to this equilibrium state, the dynamics can be approximated as $\frac{dx}{dt} \approx \lambda x + \eta$, where η denotes a stochastic forcing representing high-frequency fluctuations. The restoring rate λ can be inferred from a linear regression of dx/dt onto x for a given time window, and can thus serve as a measure of temporal stability changes. The estimated values of λ are independent of changing variance of the noise η, thus yielding an indicator that is not biased in the way that the widely used variance indicator is. However, possible changes in the autocorrelation of the noise term η can still bias the value of λ if inferred via linear regression under the assumption that η has constant autocorrelation. This regression is therefore performed with a suitable generalized least-squares algorithm under the assumption of noise with varying autocorrelation (Methods). The resulting estimate of λ is not biased by changing variance and

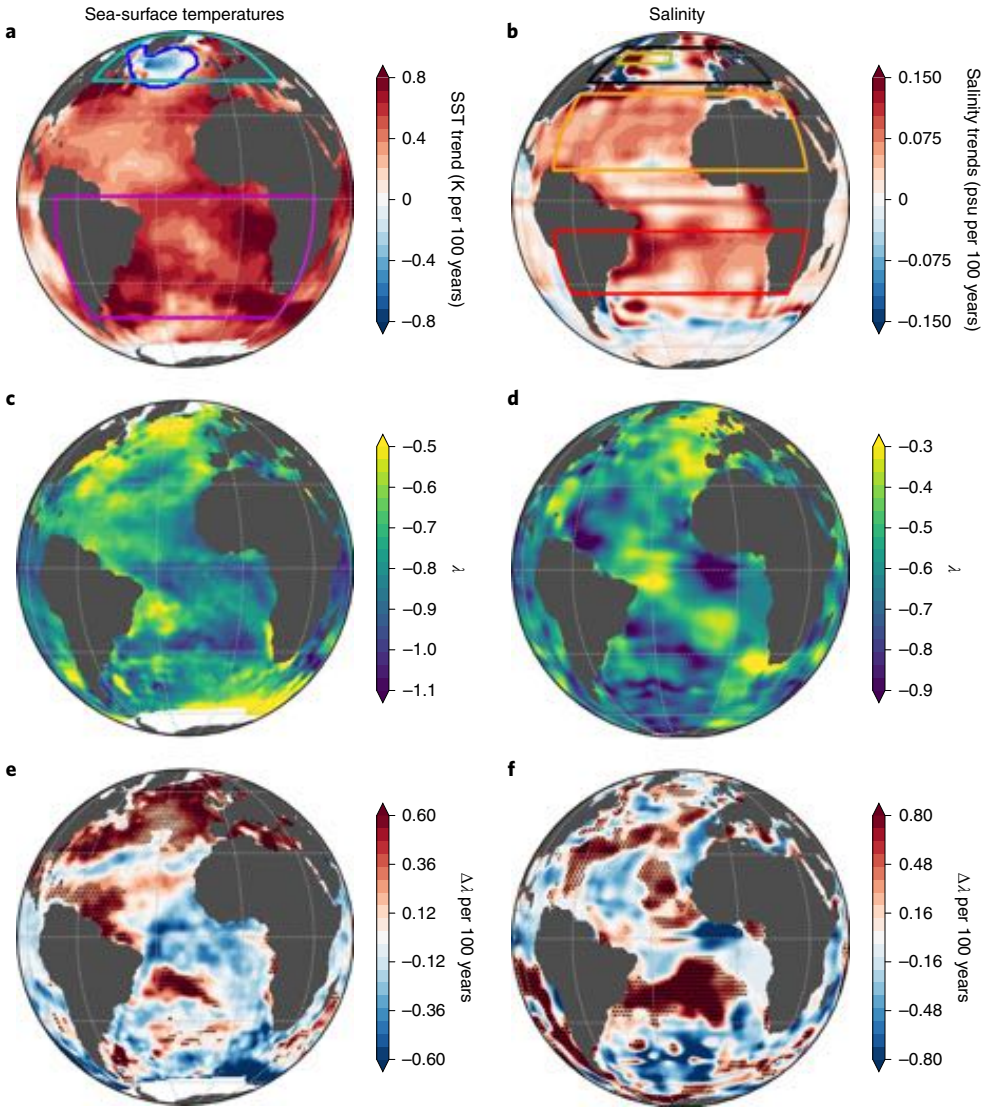

Fig. 2 | Spatial trends and EWS in Atlantic SSTs and salinity. a, Linear SST trends in the Atlantic, estimated from the HadISST dataset[54]. Coloured boxes indicate the regions used to define the different SST-based AMOC indices (Methods and Fig. 3): the subploar gyre region[30] (blue) used to define $SST_{SG\text{-}GM}$[30], $SST_{SG\text{-}GM\text{-}AMO}$ and $SST_{SG\text{-}NH}$[45], as well as the North (cyan) and South (magenta) Atlantic regions used to define SST_{DIPOLE}[11]. **b**, Linear salinity trends in the Atlantic Ocean, estimated from averages of the EN4 dataset[55] over ocean levels from 300 m to the surface. Coloured boxes indicate the regions used to define the different salinity-based AMOC indices (Methods and Fig. 3): the northern North Atlantic region used by Chen and Tung[50] (S_{NN1}, black), the smaller northern North Atlantic region proposed by Klus et al.[42] (S_{NN2}, yellow) and the North (orange) and South (red) Atlantic regions proposed by Zhu and Liu[46]. **c**, Mean restoring rate λ for the non-linearly detrended SSTs (running mean with window size $r = 50$ years), estimated under the assumption of autocorrelated noise in sliding windows of size $w = 70$ years. **d**, Same as **c** but for the non-linearly detrended salinity. **e**, Linear trend of the restoring rate λ for the SSTs. **f**, Same as **e** but for the salinity. Stippling in **e** and **f** marks regions with significantly increasing trends ($P < 0.05$, see Methods for details on the statistical test). Corresponding results for the variance and AC1 are shown in Extended Data Figs. 1 and 2.

autocorrelation of the noise η (Fig. 1 and Supplementary Fig. S1). As for the classical indicators, the formal derivation of λ as an EWS requires that the dynamics should not be too far from equilibrium; it has been shown, however, that the classical EWS indeed remain valid even in the non-equilibrium case of rate-induced transitions[38] (Methods).

The restoring rate λ is negative for stable system states, and the point where it reaches zero from below marks the bifurcation point, that is, the critical value of the control parameter where the abrupt transition will occur (Fig. 1g). This allows one to quantify the distance to the critical transition. It can moreover be shown that, if the system under study approaches a critical transition, then λ evolves inversely proportionally to the sensitivity of the system's equilibrium state to changes in the control parameter T, given by dx^*/dT. Moreover, the variance of the fluctuations around x^* increases proportionally to $|dx^*/dT|$ if a critical transition is approached[35] (Methods). These relationships between the restoring rate λ, the sensitivity dx^*/dT and the variance of fluctuations around the stable state x^* can be used to associate statistical EWS of a critical transition with the underlying physical mechanisms.

Although not directly transferable to present-day climate conditions, the AMOC bistability during glacial conditions, in combination with the AMOC bistability in simulations with comprehensive, eddy-permitting models, suggests that also the present-day AMOC may exhibit a second, substantially weaker circulation mode. In particular, the combined evidence makes it plausible that a critical

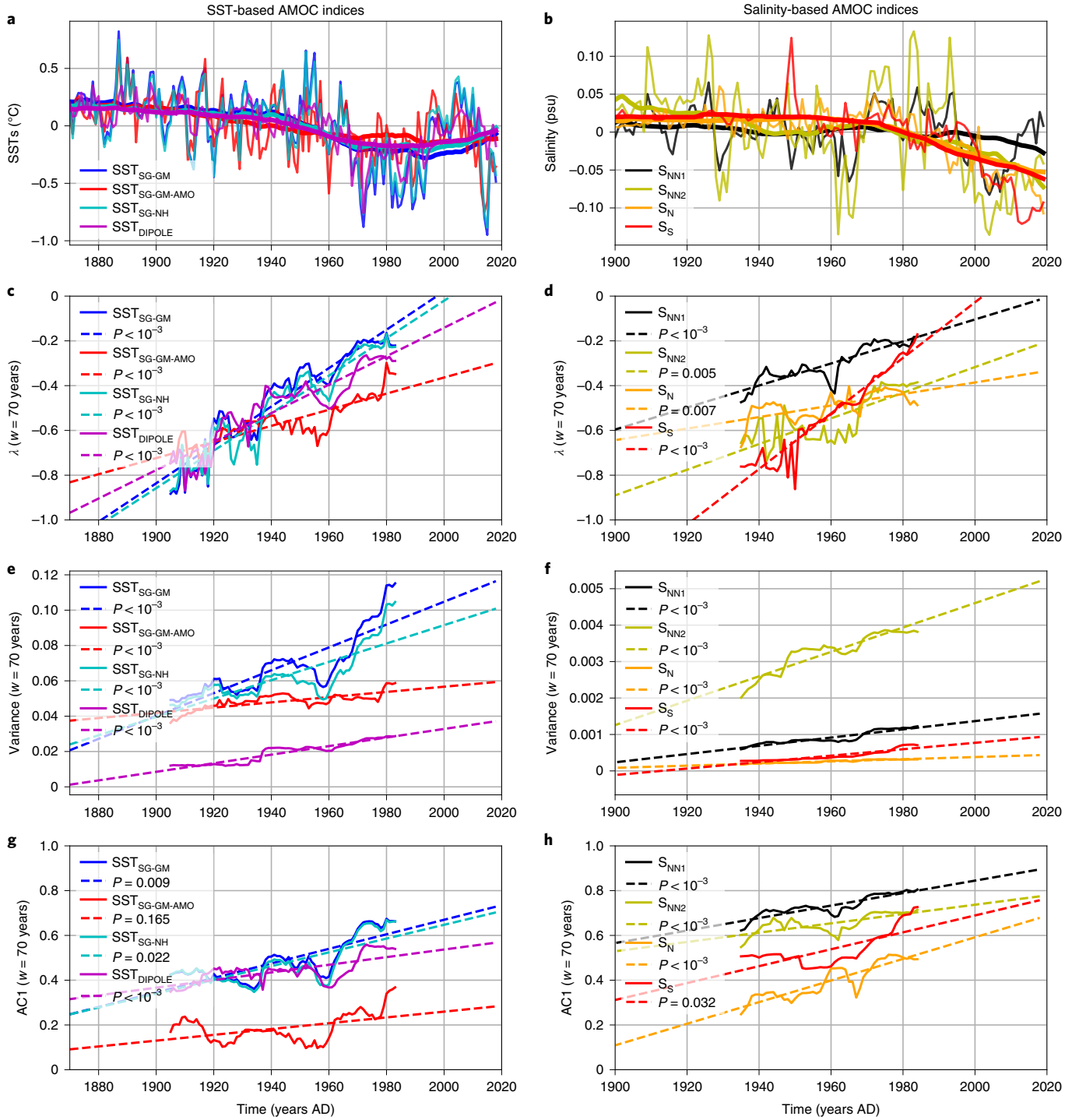

Fig. 3 | EWS for SST- and salinity-based AMOC indices. a, SST-based AMOC indices (thin) together with 50-year running means (thick). **b**, Salinity-based AMOC indices (thin) together with 50-year running means (thick). **c**, The restoring rate λ of the detrended SST-based AMOC indices, estimated under the assumption of autocorrelated noise. **d**, The restoring rate λ of the detrended salinity-based AMOC indices, estimated under the assumption of autocorrelated noise. **e**, Same as **c** but for the variance. **f**, Same as **d** but for the variance. **g**, Same as **c** but for the AC1. **h**, Same as **d** but for the AC1. Dashed lines indicate the linear trends of the three early-warning indicators, with *P* values given in the legends. Values for each sliding window are plotted at the centre point of that window. Data for the first and last $w/2 = 35$ years are omitted because no full time windows to estimate the different early-warning indicators are available there. Corresponding results using different sliding window sizes are shown in Extended Data Figs. 3 and 4.

transition to the weak mode may occur in response to rising temperatures and North Atlantic freshwater inflow. It is therefore justified to search for EWS for AMOC collapse in both model simulations and observations. EWS in terms of rising variance and lag-1 autocorrelation (AC1) prior to hosing-enforced AMOC transitions have been be identified in low-order models[39], EMICs[37,40] and fully coupled AOGCMs[41]. Recently, a spatial analysis of comprehensive model simulations revealed clear EWS prior to an AMOC collapse

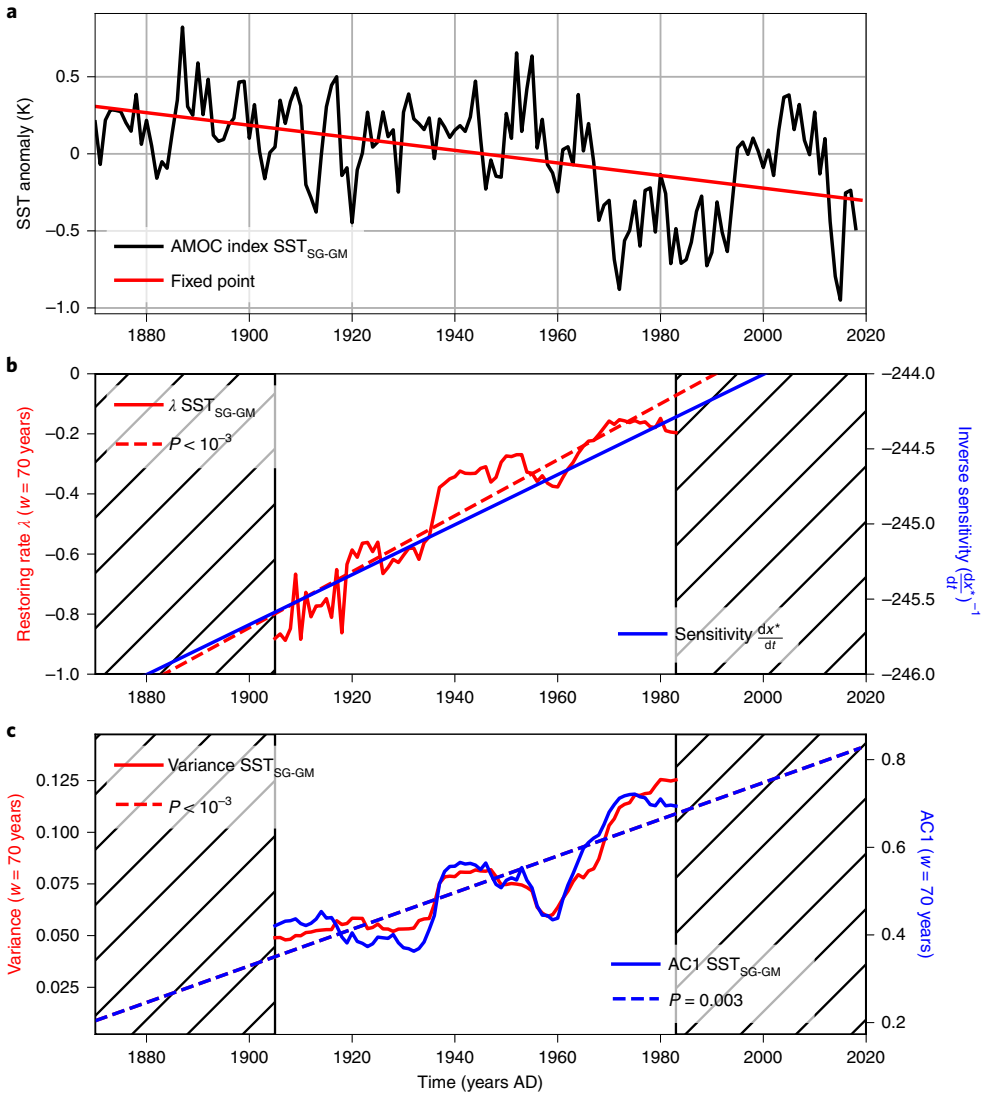

Fig. 4 | EWS for AMOC index SST_{SG-GM} with modelled fixed point. a, The SST-based AMOC index SST_{SG-GM}, constructed by subtracting the global mean SSTs from the average SSTs of the subpolar gyre region (black), and least-squares fit of the fixed point of a conceptual AMOC model (red; Methods). **b**, The restoring rate λ (red) estimated from fluctuations around the fitted fixed point under the assumption of autocorrelated residual noise, in sliding windows of width $w = 70$ years; the inverse sensitivity $(dx^*/dt)^{-1}$ of the model is shown in blue for comparison (Methods). **c**, Variance (red) and AC1 (blue), estimated from fluctuations around the fixed point. In panels **b** and **c**, dashed lines indicate the linear trends of the three early-warning indicators, with *P* values given in the legends. Note that the linear trends for variance and AC1 overlie each other in this case. Values for each sliding window are plotted at the centre point of that window. As above, data for the first and last $w/2 = 35$ years are omitted because no full time windows to estimate the different early-warning indicators are available there. Corresponding results for the other seven AMOC indices are shown in Extended Data Fig. 5.

under Holocene conditions in the sea-surface temperature (SST) and sea-surface salinity of the northern Atlantic[42]. EWS have also been revealed in the decadal frequency bands of ice-core-derived proxy time series prior to the abrupt DO events during the last glacial interval[43,44], which have been associated with AMOC transitions.

First, detrended SST and salinity time series in the Atlantic Ocean are investigated, starting in 1870 and 1900, respectively (Fig. 2). As previously reported[30,45], the only negative SST trends are found in the 'warming hole' south of Greenland (Fig. 2a), and similarly, the strongest negative salinity trends are found south of Greenland and in the Southern Ocean (Fig. 2b). The exceptional negative trends in the subpolar gyre region south of Greenland are consistent with a slowdown of the AMOC. The restoring rate λ exhibits the overall highest values for both the SST and the salinity data in the northern Atlantic, around the subpolar gyre region where the negative SST and salinity trends are found (Fig. 2c,d). For both SST and salinity time series, the linear trends of the restoring rate are strongly positive in most parts of the northern Atlantic and additionally in the southern Atlantic Ocean, where a salinity pile-up has recently been observed[46] (Fig. 2e,f). These results for the restoring rate λ are consistent with the other two EWS indicators (Extended Data Figs. 1 and 2). Although these results do not allow direct inference regarding the AMOC, they give a first indication that the Atlantic Ocean circulation system may be losing stability. A detailed analysis of observational, SST- and salinity-based AMOC indices is presented in the following.

Direct observations of AMOC strength are only available for the last two decades[47]. Although a negative trend can be inferred from these observations, their temporal coverage is not yet sufficient to infer a climatological AMOC weakening and a contribution

by anthropogenic climate change, as opposed to natural decadal fluctuations. Therefore, several fingerprints of AMOC variability, based on different spatial averages of SST and salinity time series that are available for longer periods, have been proposed and investigated[11,48–51]. Recent cooling anomalies of SSTs in the subpolar gyre region south of Greenland (Fig. 2a) have been associated with a weakening AMOC during the last decades[45]. By comparing observed SST anomaly patterns in the subpolar gyre region with shorter-term observations of AMOC strength and simulations from a suite of models from the Coupled Model Intercomparison Project (CMIP), and showing that decreases in the SST-derived indices are consistent with the reductions of AMOC strength in the models, fingerprints of a weakening AMOC over the last 150 years have been inferred[30].

Four SST-based and four salinity-based AMOC indices are considered here. The indices $SST_{SG\text{-}GM}$[30], $SST_{SG\text{-}GM\text{-}AMO}$, which is based on the same spatial regions but with the linear contribution of the Atlantic Multidecadal Oscillation (AMO) removed, as well as $SST_{SG\text{-}NH}$[45] focus on the subpolar gyre region south of Greenland, while the index SST_{DIPOLE} is constructed by subtracting South-Atlantic from North-Atlantic SSTs[11]. These indices have been shown to correlate highly with actual AMOC strength in simulations with freshwater hosing and gradual CO_2 increase, using the high-resolution, eddy-permitting HadGEM3-GC2 model[51]. Following Zhang[48] and Chen and Tung[50], a salinity-based AMOC index is constructed by averaging the salinity concentration over the North Atlantic. In addition, a smaller subset of this region south of Greenland is considered for a second salinity-based index S_{NN2} because EWS for AMOC collapse have been identified there recently in model simulations[42]. Motivated by a recently revealed salinity pile-up[46], a third and a fourth salinity-based index is constructed by averaging the salinity concentration in the North and South Atlantic basin, respectively (Methods and Figs. 2 and 3).

Almost all the non-linearly detrended SST- and salinity-based AMOC indices (Fig. 3a,b) show highly significant increases in the three considered EWS indicators ($P<0.05$, except for the AC1 of $SST_{SG\text{-}GM\text{-}AMO}$; Fig. 3c–h), providing evidence that the AMOC is approaching a bifurcation-induced transition. Statistical significance of positive trends is determined from a test based on phase surrogates that preserve both variance and autocorrelation (Methods), and the results are not sensitive to changing the size of the sliding windows (Extended Data Figs. 3 and 4). The possibility of false alarms due to rising variance or AC1 of the high-frequency forcing can be ruled out since the corrected restoring rate λ has been considered here.

To put these results into closer context with the underlying bifurcation mechanism, the fluctuations obtained by subtracting the observed AMOC indices from a modelled equilibrium state of the AMOC are investigated. A simple model capturing the bistable dynamics of the AMOC is given by a non-linear differential equation model with two different stable equilibrium states and an unstable state in between[52] (Methods). AMOC variability and in particular its bifurcation structure in comprehensive models have been shown to be in good agreement with such simplified descriptions[5,26,53]. The conceptual models imply a third-order dependence of the fixed point x^* on the control parameter T, for which the global mean SSTs are used. Assuming linearly rising global mean SSTs, this also implies a third-order dependence of x^* on time. To ensure that the EWS indicators are not biased by the statistical detrending performed for the results shown in Figs. 2 and 3, a third-order model for the fixed point x^* is hence fitted to the different AMOC indices (Fig. 4 and Extended Data Fig. 5), and the fluctuations around this fixed point are investigated. The restoring rate λ increases significantly for almost all the AMOC indices ($P<0.05$, except for the AC1 of $SST_{SG\text{-}GM\text{-}AMO}$ and S_S). As expected for a system approaching a bifurcation-induced transition, the time evolution of the restoring rate λ is strongly correlated with the inverse of the estimated model sensitivity dx^*/dt, which provides strong evidence that the AMOC is indeed approaching a critical, bifurcation-induced transition. EWS in terms of rising variance and AC1 are also found for the eight different AMOC indices (Fig. 4 and Extended Data Fig. 5).

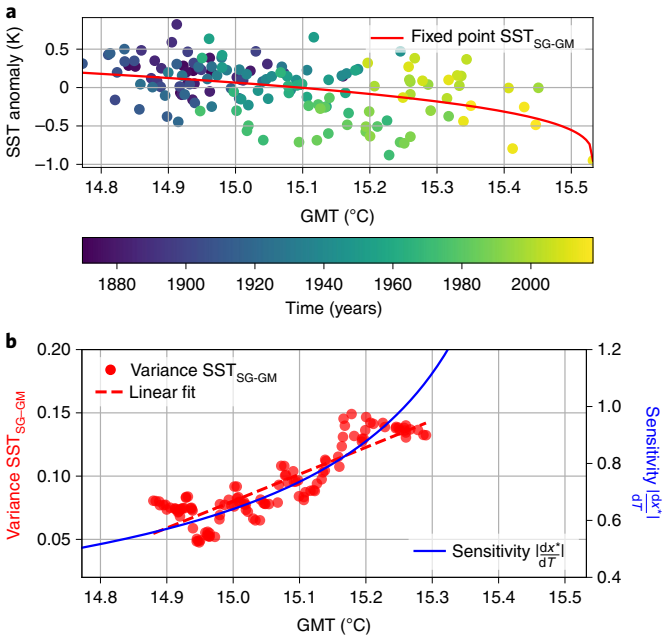

Fig. 5 | AMOC index $SST_{SG\text{-}GM}$ and EWS as functions of global mean temperature (GMT). a The SST-based AMOC $SST_{SG\text{-}GM}$ index as a function of global mean SSTs, and least-squares fit of the fixed point of a conceptual AMOC model. **b**, Variance of fluctuations of the AMOC index around the fixed point (red) and corresponding sensitivity $|dx^*/dT|$ of the model, with control parameter T given by the global mean SSTs. Values for each sliding window are plotted at the centre point of that window. Windows with fewer than 30 data points to estimate the variance are omitted. Corresponding results for the other seven AMOC indices are shown in Extended Data Fig. 6.

One may argue that the control parameter T, given by the global mean SSTs, does not increase strictly linearly in time. Therefore, to further confirm the above results, the different AMOC indices are investigated directly as functions of the global mean SSTs (Fig. 5a and Extended Data Fig. 6). The variance of fluctuations around the fixed point increases as a function of the global mean SSTs, in close relationship with the absolute value of the model sensitivity $|dx^*/dT|$ (Fig. 5b) as expected for a destabilizing AMOC on the way to a critical transition (Methods). These results are robust across the eight different AMOC indices (Extended Data Fig. 6). Note that the fact that the theoretically expected relationships between variance and λ on the one hand, and the sensitivity dx^*/dT on the other hand, hold true for the empirical AMOC indices indicates that the dynamics is indeed not too far from equilibrium.

Using three different indicators, highly significant EWS for an abrupt AMOC transition in four SST- and four salinity-based AMOC indices, covering the time spans from 1870 to 2019 and 1900 to 2019, respectively, are thus revealed. The restoring rate λ has evolved almost linearly from values close to −1 to values close to 0 over the course of the last century. Since $\lambda=0$ marks the bifurcation point at which the critical transition is expected to occur, these results provide empirical evidence that the AMOC is now close to a critical transition. The fact that significant increases of the corrected restoring rate λ proposed here are obtained rules out that the revealed EWS are caused by corresponding changes in the external noise forcing. In addition to the robustness in terms of different

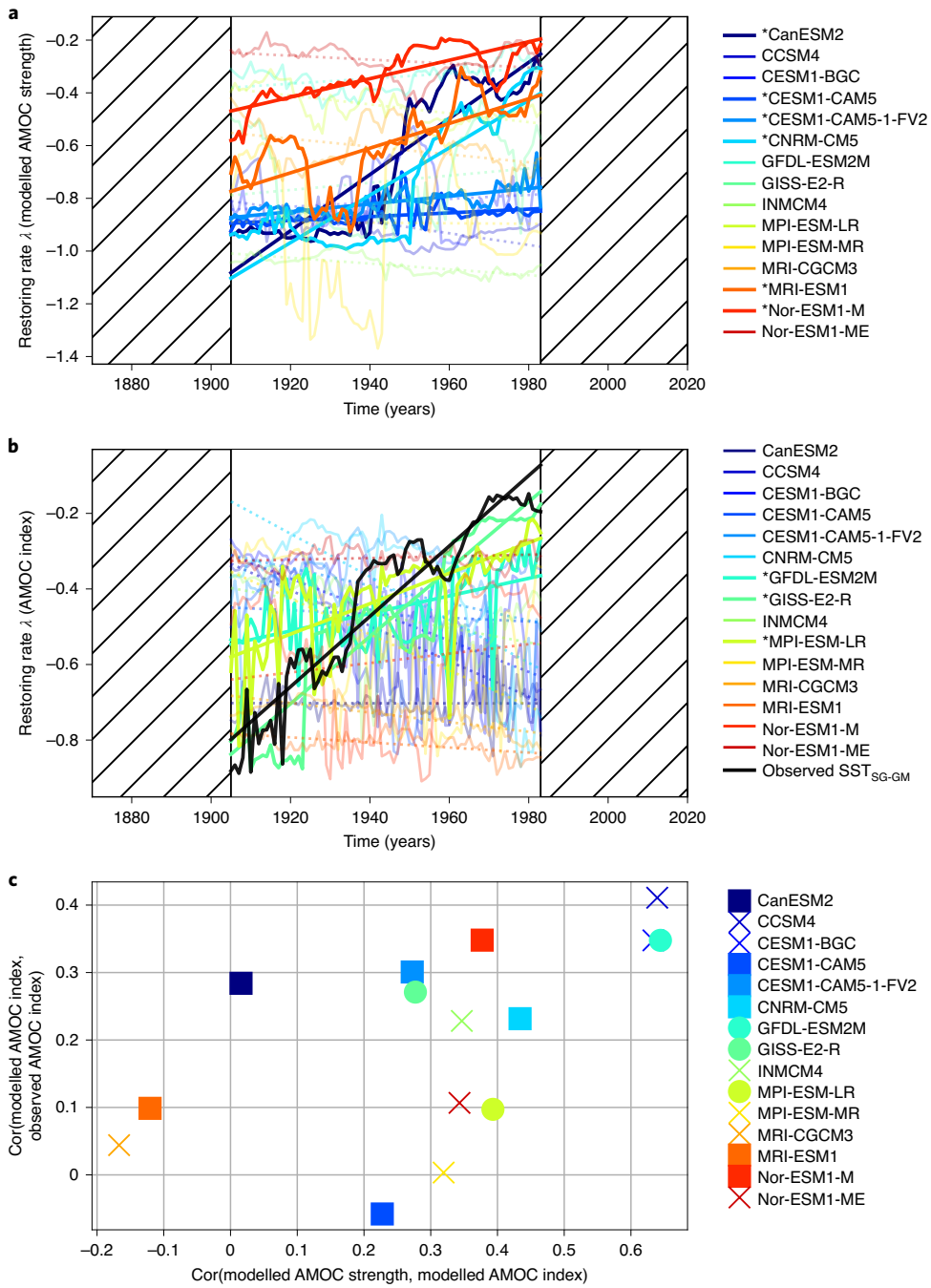

Fig. 6 | AMOC strength and SST-based index in CMIP5 models. a, The restoring rate λ computed for the AMOC strength ψ as modelled by 15 different CMIP5 models. Models that exhibit significant ($P<0.05$) increases of λ are indicated by an asterisk in the legend. **b**, Same as **a** but for the SST-based AMOC index $SST_{SG\text{-}GM}$ as simulated by the different models[30]. The observation-based AMOC index (black solid) is shown for comparison. **c**, Correlation between the modelled and observed AMOC index versus the correlation between modelled AMOC strength and modelled SST-based AMOC index. Crosses indicate that neither the modelled AMOC strength nor the modelled AMOC index exhibit significant increases of λ, squares indicate that the modelled AMOC strength exhibits significant ($P<0.05$) increases of λ and circles indicate that the modelled SST-based AMOC index exhibits significant ($P<0.05$) increases of λ.

AMOC indices, the presented results are also robust against different detrending and detection methods (Figs. 3–5), the choice of the sliding window size (Extended Data Figs. 3, 4, 7 and 8) and the SST dataset employed (Extended Data Fig. 9) (Methods).

Corresponding EWS in terms of the restoring rate λ are found in only a subset of the historical simulations of the CMIP5 models. For the modelled AMOC strength, quantified as the maximum strength over all ocean depth at 26° N, 6 out of 15 models yield simulations with significant ($P<0.05$) increases of λ in the period 1870–2018 (Fig. 6a). For the modelled SST-based AMOC index, derived in the same way as the observed one by subtracting subpolar gyre SSTs from the global mean[30], significantly ($P<0.05$) increasing λ are only found in 3 out of the 15 investigated models (Fig. 6b). None of the models exhibit significantly increasing λ for both the modelled AMOC strength and the modelled SST-based index. Notably, from the three models with highest correlations between modelled

AMOC strength and modelled SST-based AMOC index, as well as highest correlations between the modelled SST-based index and the observed SST-based index, only one (GFDL-ESM2M) exhibits significant increases of the restoring rate λ for the modelled SST-based AMOC index (Fig. 6c). Similar results are obtained when considering the maximum modelled AMOC strength over all ocean depths from 20° N to 60° N (Extended Data Fig. 10). At a confidence level of 0.05, one would expect to obtain an apparently significant positive trend in only 1 out of 20 test realizations by chance, if there were in fact no underlying trend. Although higher numbers of significant EWS are obtained for the CMIP models, these findings still raise concern regarding whether state-of-the-art climate models would be skilful in predicting a forthcoming AMOC collapse. This is in agreement with previous results showing that the present AMOC mode is too stable in state-of-the-art models[9], most likely due to an underestimation of the freshwater export from the northern Atlantic Ocean, caused by errors in the salinity fields and insufficient model resolution[12]. The high-resolution, eddy-permitting HadGEM3-GC2 model, which was used to establish the suitability of the SST-based AMOC indices employed here[51], constitutes a major step forward concerning a more accurate representation of the AMOC and its stability[12,14]. A continuous evaluation of new model versions in terms of AMOC indices and their EWS will be subject to future research. In particular, for models with excessively stable AMOC, one would not expect to observe EWS, and the results presented here could therefore be used to identify observational constraints for climate models.

In simulations with a coupled AOGCM with hosing-enforced AMOC collapse, EWS in terms of rising variance and AC1 have been revealed[41]. The evolution of the AC1 prior to AMOC collapse in the simulations of the latter study (see fig. 4c there) is very similar to the evolution of the AC1 of the observation-based indices investigated here (Figs. 3g,h and 4c and Extended Data Figs. 3g,h, 4g,h, 5g,h, 7g,h and 8g,h). The EWS revealed here for observation-based AMOC indices thus behave exactly like corresponding signals in comprehensive model simulations prior to an AMOC collapse. Note that, in the model hosing experiment[41], the AMOC collapses even before the AC1 reaches the critical value $AC1_c = 1$ (corresponding to $\lambda_c = 0$; Methods) because the fluctuations push the AMOC out of the weakly stable state already before it ceases to exist. Similar observations have been made also in more recent hosing experiments[53].

The results presented here hence show that the recently discovered AMOC decline during the last decades is not just a fluctuation related to low-frequency climate variability or a linear response to increasing temperatures. Rather, the presented findings suggest that this decline may be associated with an almost complete loss of stability of the AMOC over the course of the last century, and that the AMOC could be close to a critical transition to its weak circulation mode.

Online content

Any methods, additional references, Nature Research reporting summaries, source data, extended data, supplementary information, acknowledgements, peer review information; details of author contributions and competing interests; and statements of data and code availability are available at https://doi.org/10.1038/s41558-021-01097-4.

Received: 17 August 2020; Accepted: 9 June 2021;
Published online: 5 August 2021

References

1. Rahmstorf, S. Ocean circulation and climate during the past 120,000 years. *Nature* **419**, 207–214 (2002).
2. Lenton, T. M. et al. Tipping elements in the Earth's climate system. *Proc. Natl Acad. Sci. USA* **105**, 1786–1793 (2008).
3. Stommel, H. Thermohaline convection with two stable regimes of flow. *Tellus* **13**, 224–230 (1961).
4. Manabe, S. & Stouffer, R. J. Two stable equilibria of a coupled ocean–atmosphere model. *J. Clim.* **1**, 841–866 (1988).
5. Rahmstorf, S. et al. Thermohaline circulation hysteresis: a model intercomparison. *Geophys. Res. Lett.* **32**, L23605 (2005).
6. Hawkins, E. et al. Bistability of the Atlantic overturning circulation in a global climate model and links to ocean freshwater transport. *Geophys. Res. Lett.* **38**, 1–6 (2011).
7. Liu, W., Liu, Z. & Brady, E. C. Why is the AMOC monostable in coupled general circulation models? *J. Clim.* **27**, 2427–2443 (2014).
8. Valdes, P. Built for stability. *Nat. Geosci.* **4**, 414–416 (2011).
9. Liu, W., Xie, S.-P., Liu, Z. & Zhu, J. Overlooked possibility of a collapsed Atlantic Meridional Overturning Circulation in warming climate. *Sci. Adv.* **3**, e1601666 (2017).
10. Drijfhout, S. S., Weber, S. L. & van der Swaluw, E. The stability of the MOC as diagnosed from model projections for pre-industrial, present and future climates. *Clim. Dyn.* **37**, 1575–1586 (2011).
11. Roberts, C. D., Garry, F. K. & Jackson, L. C. A multimodel study of sea surface temperature and subsurface density fingerprints of the Atlantic meridional overturning circulation. *J. Clim.* **26**, 9155–9174 (2013).
12. Mecking, J. V., Drijfhout, S. S., Jackson, L. C. & Andrews, M. B. The effect of model bias on Atlantic freshwater transport and implications for AMOC bi-stability. *Tellus A* **69**, 1–15 (2017).
13. Weijer, W., Maltrud, M. E., Hecht, M. W., Dijkstra, H. A. & Kliphuis, M. A. Response of the Atlantic Ocean circulation to Greenland Ice Sheet melting in a strongly-eddying ocean model. *Geophys. Res. Lett.* **39**, L09606 (2012).
14. Jackson, L. C. & Wood, R. A. Hysteresis and resilience of the AMOC in an eddy-permitting GCM. *Geophys. Res. Lett.* **45**, 8547–8556 (2018).
15. Henry, L. G. North Atlantic ocean circulation and abrupt climate change during the last glaciation. *Science* **353**, 470–474 (2016).
16. Boers, N., Ghil, M. & Rousseau, D.-D. Ocean circulation, ice shelf, and sea ice interactions explain Dansgaard–Oeschger cycles. *Proc. Natl Acad. Sci. USA* **115**, E11005–E11014 (2018).
17. Wang, Y. et al. Millennial- and orbital-scale changes in the East Asian monsoon over the past 224,000 years. *Nature* **451**, 18–21 (2008).
18. Kanner, L. C., Burns, S. J., Cheng, H. & Edwards, R. L. High-latitude forcing of the South American summer monsoon during the last glacial. *Science* **335**, 570–573 (2012).
19. Mosblech, N. A. et al. North Atlantic forcing of Amazonian precipitation during the last ice age. *Nat. Geosci.* **5**, 817–820 (2012).
20. Zhang, X., Lohmann, G., Knorr, G. & Purcell, C. Abrupt glacial climate shifts controlled by ice sheet changes. *Nature* **512**, 290–294 (2014).
21. Vettoretti, G. & Peltier, W. R. Thermohaline instability and the formation of glacial North Atlantic super polynyas at the onset of Dansgaard–Oeschger warming events. *Geophys. Res. Lett.* **43**, 5336–5344 (2016).
22. Klockmann, M., Mikolajewicz, U., Kleppin, H. & Marotzke, J. Coupling of the subpolar gyre and the overturning circulation during abrupt glacial climate transitions. *Geophys. Res. Lett.* **47**, e2020GL090361 (2020).
23. Stocker, T. F. & Wright, D. G. Rapid transitions of the ocean's deep circulation induced by changes in surface water fluxes. *Nature* **351**, 729–732 (1991).
24. Vellinga, M. & Wood, R. A. Global climatic impacts of a collapse of the atlantic thermohaline circulation. *Climatic Change* **54**, 251–267 (2002).
25. Stouffer, R. J. et al. Investigating the causes of the response of the thermohaline circulation to past and future climate changes. *J. Clim.* **19**, 1365–1387 (2006).
26. Wood, R. A., Rodríguez, J. M., Smith, R. S., Jackson, L. C. & Hawkins, E. Observable, low-order dynamical controls on thresholds of the Atlantic meridional overturning circulation. *Clim. Dyn.* **53**, 6815–6834 (2019).
27. Vellinga, M. & Wood, R. A. Impacts of thermohaline circulation shutdown in the twenty-first century. *Climatic Change* **91**, 43–63 (2008).
28. Kageyama, M. et al. Climatic impacts of fresh water hosing under last glacial maximum conditions: a multi-model study. *Clim. Past* **9**, 935–953 (2013).
29. Gierz, P., Lohmann, G. & Wei, W. Response of Atlantic overturning to future warming in a coupled atmosphere–ocean–ice sheet model. *Geophys. Res. Lett.* **42**, 6811–6818 (2015).
30. Caesar, L., Rahmstorf, S., Robinson, A., Feulner, G. & Saba, V. Observed fingerprint of a weakening Atlantic Ocean overturning circulation. *Nature* **556**, 191–196 (2018).
31. Jackson, L. C. et al. Global and European climate impacts of a slowdown of the AMOC in a high resolution GCM. *Clim. Dyn.* **45**, 3299–3316 (2015).
32. Dakos, V. et al. Slowing down as an early warning signal for abrupt climate change. *Proc. Natl Acad Sci. USA* **105**, 14308–14312 (2008).
33. Scheffer, M. et al. Early-warning signals for critical transitions. *Nature* **461**, 53–59 (2009).
34. Lenton, T. M. Early warning of climate tipping points. *Nat. Clim. Change* **1**, 201–209 (2011).

35. Boers, N. & Rypdal, M. Critical slowing down suggests that the western Greenland Ice Sheet is close to a tipping point. *Proc. Natl Acad. Sci. USA* **118**, e2024192118 (2021).
36. Bathiany, S. et al. Beyond bifurcation: using complex models to understand and predict abrupt climate change. *Dyn. Stat. Clim.* **1**, dzw004 (2016).
37. Held, H. & Kleinen, T. Detection of climate system bifurcations by degenerate fingerprinting. *Geophys. Res. Lett.* https://doi.org/10.1029/2004GL020972 (2004).
38. Ritchie, P. & Sieber, J. Early-warning indicators for rate-induced tipping. *Chaos* https://doi.org/10.1063/1.4963012 (2016).
39. Kleinen, T., Held, H. & Petschel-Held, G. The potential role of spectral properties in detecting thresholds in the Earth system: application to the thermohaline circulation. *Ocean Dyn.* **53**, 53–63 (2003).
40. Lenton, T. M. et al. Using GENIE to study a tipping point in the climate system. *Phil. Trans. R. Soc. A* **367**, 871–884 (2008).
41. Boulton, C. A., Allison, L. C. & Lenton, T. M. Early warning signals of Atlantic Meridional Overturning Circulation collapse in a fully coupled climate model. *Nat. Commun.* **5**, 5752 (2014).
42. Klus, A., Prange, M., Varma, V. & Schulz, M. Spatial analysis of early-warning signals for a North Atlantic climate transition in a coupled GCM. *Clim. Dyn.* **53**, 97–113 (2019).
43. Rypdal, M. Early-warning signals for the onsets of Greenland interstadials and the younger dryas-preboreal transition. *J. Clim.* **29**, 4047–4056 (2016).
44. Boers, N. Early-warning signals for Dansgaard–Oeschger events in a high-resolution ice core record. *Nat. Commun.* **9**, 2556 (2018).
45. Rahmstorf, S. et al. Exceptional twentieth-century slowdown in Atlantic Ocean overturning circulation. *Nat. Clim. Change* **5**, 475–480 (2015).
46. Zhu, C. & Liu, Z. Weakening Atlantic overturning circulation causes South Atlantic salinity pile-up. *Nat. Clim. Change* **10**, 998–1003 (2020).
47. Smeed, D. A. et al. The north Atlantic Ocean is in a state of reduced overturning. *Geophys. Res. Lett.* **45**, 1527–1533 (2018).
48. Zhang, R. On the persistence and coherence of subpolar sea surface temperature and salinity anomalies associated with the Atlantic multidecadal variability. *Geophys. Res. Lett.* **44**, 7865–7875 (2017).
49. Alexander-Truner, R., Ortega, P. & Robson, J. I. How robust are the surface temperature fingerprints of the Atlantic Overturning Meridional Circulation on monthly time scales? *Geophys. Res. Lett.***45**, 3559–3567 (2018).
50. Chen, X. & Tung, K. K. Global surface warming enhanced by weak Atlantic overturning circulation. *Nature* **559**, 387–391 (2018).
51. Jackson, L. C. & Wood, R. A. Fingerprints for early detection of changes in the AMOC. *J. Clim.* **33**, 7027–7044 (2020).
52. Cessi, P. A simple box model of stochastically forced thermohaline flow. *J. Phys. Oceanogr.* **24**, 1911–1920 (1994).
53. Alkhayuon, H., Ashwin, P., Jackson, L. C., Quinn, C. & Wood, R. A. Basin bifurcations, oscillatory instability and rate-induced thresholds for Atlantic meridional overturning circulation in a global oceanic box model. *Proc. R. Soc. A* **475**, 20190051 (2019).
54. Rayner, N. A. Global analyses of sea surface temperature, sea ice, and night marine air temperature since the late nineteenth century. *J. Geophys. Res.* **108**, 4407 (2003).
55. Good, S. A., Martin, M. J. & Rayner, N. A. EN4: quality controlled ocean temperature and salinity profiles and monthly objective analyses with uncertainty estimates. *J. Geophys. Res.* **118**, 6704–6716 (2013).

Methods

Derivation of SST- and salinity-based AMOC indices. *SST-based indices.* Following Rahmstorf et al.[45] and Caesar et al.[30], the set of SST grid cells in the North Atlantic is used that exhibits relative cooling when normalized to the global mean SST trend in either the HadISST reanalysis data[54] or the simulations of a CO_2 doubling experiment of the GFDL CM2.6 climate model (blue contour in Fig. 2a; note that the presented results are not sensitive to small variations of this region). Thereafter, the average over this subpolar gyre region for each November–May season is taken, and the global mean SSTs is subtracted to obtain the AMOC index $SST_{SG\text{-}GM}$ as proposed by Caesar et al.[30]. Since the decadal variability of this AMOC index is closely related to the AMO, a simple linear regression of the AMOC index onto the AMO is performed, and the residual is taken as a modified AMOC index $SST_{SG\text{-}GM\text{-}AMO}$ for comparison. For the latter case, the AMO index is computed following Trenberth et al.[56] as the difference between mean North Atlantic (0–80° N) SSTs and global mean SSTs, normalized by the mean difference for the time period 1900–1970. For the third SST-based index $SST_{SG\text{-}NH}$, the mean subpolar gyre SSTs are taken, and the Northern-Hemisphere mean is subtracted, as originally proposed by Rahmstorf et al.[45]. Finally, the index SST_{DIPOLE}, originally proposed by Roberts et al.[11], is constructed by subtracting SSTs in the South Atlantic region defined by 0–45° S, 70° W to 30° E from SSTs in the North Atlantic region defined by 45–80° N, 70° W to 30° E. The three indices $SST_{SG\text{-}GM}$, $SST_{SG\text{-}GM\text{-}AMO}$ and SST_{DIPOLE} have been shown to correlate highly with the actual AMOC strength in simulations of the high-resolution, eddy-permitting coupled climate model HadGEM3-GC2 (ref. [51]).

Salinity-based indices. Following Zhang[48] and Chen and Tung[50], the salinity-based AMOC index S_{NN1} is constructed by averaging the salinity content of the Atlantic Ocean basin from 45° N to 65° N using the EN4 dataset[55]. Also, a smaller subset of the northern North Atlantic region (54–62° N, 26–62° W) is taken for a second salinity-based index S_{NN2}, because EWS for an AMOC collapse have been identified in this region in model simulations recently[42]. Motivated by the results of Zhu and Liu[46], the salinity concentration in the North Atlantic basin from 10° N to 40° N is averaged to obtain the index S_N. Finally, a salinity pile-up in the South Atlantic has recently been revealed and associated with the slowing of the AMOC over recent decades[46]. Accordingly, a South Atlantic AMOC index is considered by averaging salinity over the Atlantic basin from 10° S to 34° S (S_S) (Figs. 2b and 3b). All salinity indices are obtained by averaging over ocean levels from 300 m to the surface and multiplying by −1 (ref. [46]).

Robust precursor signals for critical transitions. *Early-warning signals.* Consider a random non-linear dynamical system described by the following equation of motion:

$$\frac{\mathrm{d}x}{\mathrm{d}t} = -U'(x;T) + \eta(t)\,,$$

where x denotes the time-dependent state variable of the system and U a potential that exhibits two minima (that is, stable equilibria or fixed points) for intermediate values of the control parameter T, but only one minimum for p outside a given range. For example, for $U(x;T) = \frac{x^4}{4} - \frac{x^2}{2} + Tx$, leading to the equation of motion $\mathrm{d}x/\mathrm{d}t = -x^3 + x - T + \eta(t)$, there would be two minima for $-\frac{2}{3\sqrt{3}} < T < \frac{2}{3\sqrt{3}}$ and only one minimum for T outside this range. The minima of U, corresponding to the possible stable equilibria of the system (where $\mathrm{d}x/\mathrm{d}t = 0$), are also called stable equilibrium or fixed points, while the relative maximum between the two minima (where also $\mathrm{d}x/\mathrm{d}t = 0$) is referred to as an unstable equilibrium or fixed point. The critical values of T at which the number of stable equilibrium points changes are the bifurcation points. The above system is driven by an external random forcing η, whose variance and autocorrelation may change over time.

The loss of stability of an equilibrium state of a non-linear dynamical system (that is, one of the minima of U in the example above) is associated with a widening of the corresponding potential well. At the bifurcation, the stable fixed point and the associated potential well eventually cease to exist, causing the system to transition rapidly to an alternative stable state. The widening of the potential well leads to weaker restoring forces (observe U' in the equation above) in response to external (random) perturbations given by η, and correspondingly slower recovery times. These characteristics give rise to the notion of 'critical slowing down'. In such idealized systems, this critical slowing down is accompanied by increases in variance (because of weaker restoring forces in response to perturbations) and autocorrelation (because of slower recovery times from perturbed states) of the time series encoding the dynamics of x. These statistical EWS preceding abrupt transitions have been discovered in many natural systems[32,33,57].

It may happen, however, that the variance and autocorrelation of η increase due to external reasons unrelated to critical slowing down, which would in turn cause increasing variance and autocorrelation in the time series of x, leading to a false alarm of a forthcoming transition (Fig. 1, right column). A different indicator for destabilization and the associated critical slowing down is therefore proposed here. For x in the vicinity of a stable fixed point x^*, the potential U can be approximated by a quadratic function, leading to the following approximate equation of motion for the fluctuations around the stable fixed point ($\Delta x = x - x^*$):

$$\frac{\mathrm{d}\Delta x}{\mathrm{d}t} \approx \lambda \Delta x + \eta(t)\,,$$

where $\lambda < 0$ if the fixed point is stable. For white noise η with constant variance, this defines an additive Ornstein–Uhlenbeck process with restoring rate λ, which corresponds to the steepness of the corresponding quadratic approximation of the potential around the fixed point. The value of λ thus directly quantifies the stability of the system[37]. Similar observations have been made in discrete settings in the context of epidemic outbreaks[58]. Within a given time window, the derivative $\mathrm{d}x/\mathrm{d}t$ can be estimated from the time series of x, and linearly regressing $\mathrm{d}x/\mathrm{d}t$ onto x yields a direct estimate of the restoring rate λ. As long as η is white, Gaussian noise, the estimate of λ is not biased by changing variance of η. However, if η is given by red noise with autocorrelation changing over time (which is indeed a very realistic assumption for the case of climate variability), a linear regression of $\mathrm{d}x/\mathrm{d}t$ onto x, using a least-squares algorithm assuming white noise, will lead to biases in the estimation of λ (Fig. 1, right column). The regression of $\mathrm{d}x/\mathrm{d}t$ onto x is therefore performed under the assumption of autocorrelated residual noise with the autoregression coefficient as a free parameter. Using this estimation for λ yields an indicator that is not sensitive to increasing variance or autocorrelation of η (Fig. 1, right column) but provides a robust warning if the system is indeed approaching a critical, bifurcation-induced transition (Fig. 1, left column).

The discretization of the Ornstein–Uhlenbeck process (with time step Δt equal to 1 year for the case at hand) gives an order-one autoregressive process with variance

$$\langle \Delta x^2 \rangle = \frac{\sigma^2}{1 - \mathrm{e}^{2\lambda \Delta t}}$$

and autocorrelation function

$$\alpha_n = \mathrm{e}^{n\lambda \Delta t}\,.$$

With $\lambda < 0$ approaching zero from below on the way to the critical transition, the variance will thus diverge to $+\infty$ and the AC1 (that is, α_1) will increase toward 1, which explains why these statistical indicators can serve to detect critical slowing down under the assumption that the statistical properties of η remain constant. Note that these relationships of $\langle \Delta x^2 \rangle$ and α_n with λ are the theoretical motivation for using variance and AC1 as EWS; the restoring rate λ should thus be preferred because it yields a more direct, and unbiased, estimate of critical slowing down and destabilization.

Note that the above formal derivation of the EWS indicators $\langle \Delta x^2 \rangle$, α_n and λ relies on the assumption that the dynamics is close to the equilibrium, and hence that the linearized dynamics of the fluctuations around the equilibrium can be considered. However, it has been shown that, even in the extreme non-equilibrium case of so-called rate-induced transitions, EWS in terms of delayed rising variance and autocorrelation arise[38].

Sensitivity. Consider a general equation of motion of the form

$$\frac{\mathrm{d}x}{\mathrm{d}t} = f(x) - T + \eta(t)$$

with a non-linear function f (which is given by $f(x) = -x^3 + x$ in the above example of a double-well system) and control parameter T. Linearization around a fixed point x^* yields for the fluctuations $\Delta x = x - x^*$

$$\frac{\mathrm{d}\Delta x}{\mathrm{d}t} = f'(x^*)\Delta x + \eta(t)$$

and hence, comparing with the above, $\lambda = f'(x^*)$. On the other hand, since by definition $\mathrm{d}x/\mathrm{d}t = 0$ at $x = x^*$ and thus $f(x^*) = T$, for the sensitivity it holds that

$$\frac{\mathrm{d}x^*}{\mathrm{d}T} = \frac{1}{f'(x^*)}.$$

Therefore, if a non-linear system of the above form is approaching a bifurcation, it should be theoretically expected that

$$\lambda \propto \left(\frac{\mathrm{d}x^*}{\mathrm{d}T}\right)^{-1}$$

as observed in Fig. 4b and Extended Data Fig. 9 (assuming an approximately linear relationship between time t and the control parameter T). Moreover, since for the locally linearized and discretized system the variance is approximately proportional to $\sigma^2/(-2\lambda)$ (recall that $\lambda < 0$ and in the given case $\Delta t = 1$), for the fluctuations around x^* it holds that[35]

$$\langle \Delta x^2 \rangle \propto \left|\frac{\mathrm{d}x^*}{\mathrm{d}T}\right|$$

as observed in Fig. 4c. The consistency of the behaviour of the restoring rate λ and the variance $\langle \Delta x^2 \rangle$ with the behaviour of the sensitivity dx^*/dT provides strong evidence of a forthcoming critical transition because the above relationships would not hold without a destabilization of the system.

Testing statistical significance of increasing trends. A widely used test to assess the statistical significance of trends is the Mann–Kendall test. This test, however, assumes identically and independently distributed data points. Given that precursor signals for critical transitions (such as variance, AC1 or the restoring rate λ proposed here) are estimated via sliding windows across the time series under study, serial correlations have to be accounted for and the Mann–Kendall test is not applicable. A different significance test, based on surrogates that preserve both the variance and the autocorrelation function of the original time series[32,43,44,59], is therefore employed here. These surrogates are constructed by first computing the Fourier transform of the underlying time series, and then randomizing the phases. Statistical significance of trends is then estimated from the statistics of linear trends obtained from 100,000 such surrogates. The significance of the increasing trends of the EWS indicators is therefore tested, rather than the significance of their individual values[60]. The minimum number of data points to infer statistically significant EWS depends strongly on the specific statistical test, but of course also on the strength of the signal and the specific dynamics in each individual case.

Conceptual AMOC model. Conceptual models of the AMOC commonly exhibit two stable states[3,52], and effectively, the dynamics can be described by a fourth-order potential with two minima, as introduced above. The corresponding bifurcation diagrams, which depict the stable fixed points as functions of the control parameter T, exhibit a stable branch corresponding to the strong AMOC mode. This branch can be approximated by a third-order function of the form $f(x) = p_0 + (-p_1(x - p_2))^{1/3}$ for arbitrary p_0 and positive p_1 and p_2. To obtain the best-suited fixed-point curve as a function of the control parameter T (under the assumption that the dynamics is not too far from equilibrium) an ordinary least-squares fit of the function f to the eight different AMOC indices is performed (Fig. 5a (red) and Extended Data Figs. 5, 7 and 8). The fluctuations of the AMOC indices around their fixed points are then computed, and EWS are searched for in these fluctuations. Note that, for the results shown in Fig. 4, a linear relationship between time and the control parameter T has been assumed.

Sensitivity of results. To rule out the possibility that the significant indicators for a destabilization of the AMOC are caused by changes in the decadal frequency variability of the AMO, a version of the SST-based AMOC index introduced in ref. [30] is considered, for which AMO variability is removed via linear regression ($SST_{SG\text{-}GM\text{-}AMO}$). See the derivation of the different indices above.

The presented results are insensitive to the specific method used for detrending the underlying AMOC indices. Figure 3 and Extended Data Figs. 3 and 4 show results for non-linearly detrended time series using a running mean filter with size $r = 50$ years, while Fig. 4 and Extended Data Fig. 5 show results for non-linearly detrended time series using the best estimate of the fixed point of a simplified AMOC model. Moreover, investigating the EWS directly as functions of the control parameter T, rather than as functions of time, yields equivalent results (compare Fig. 4 with Fig. 5).

The choice of the window size used to estimate changes in the EWS indicators variance, AC1 and restoring rate λ is determined by a trade-off between having sufficient data points in each window to estimate the different indicators reliably and having sufficient data points in total, obtained from each window, to estimate trends reliably. In the main text, results using a window size $w = 70$ years are shown. These remain very similar when using window sizes ranging from $w = 60$ years to $w = 80$ years (Extended Data Figs. 3 and 4 or 7 and 8).

Very similar results for the SST-based index, in terms of significant indicators for an ongoing destabilization of the AMOC, are obtained when using the ERSST[61] instead of HadISST dataset (Extended Data Fig. 9).

Data availability

The HadISST reanalysis data used here are publicly available at https://www.metoffice.gov.uk/hadobs/hadisst/. The CMIP5 data are publicly available at https://esgf-node.llnl.gov/projects/cmip5/. The grid cells used to define the subpolar gyre region can be downloaded from http://www.pik-potsdam.de/~caesar/AMOC_slowdown/. Ocean salinity data can be obtained from https://www.metoffice.gov.uk/hadobs/en4/.

Code availability

All Python code used for the analysis is available from the author upon request (boers@pik-potsdam.de) or on GitHub at https://github.com/niklasboers/AMOC_EWS.

References

56. Trenberth, K. E. & Shea, D. J. Atlantic hurricanes and natural variability in 2005. *Geophys. Res. Lett.* **33**, 1–4 (2006).
57. Dakos, V., Nes, E. H. & Scheffer, M. Flickering as an early warning signal. *Theor. Ecol.* **6**, 309–317 (2013).
58. Rypdal, M. & Sugihara, G. Inter-outbreak stability reflects the size of the susceptible pool and forecasts magnitudes of seasonal epidemics. *Nat. Commun.* **10**, 2374 (2019).
59. Dakos, V. et al. Methods for detecting early warnings of critical transitions in time series illustrated using simulated ecological data. *PLoS ONE* **7**, e41010 (2012).
60. Ditlevsen, P. D. & Johnsen, S. J. Tipping points: early warning and wishful thinking. *Geophys. Res. Lett.* **37**, 2–5 (2010).
61. Huang, B. et al. Extended reconstructed sea surface temperature, version 5 (ERSSTv5): upgrades, validations, and intercomparisons. *J. Clim.* **30**, 8179–8205 (2017).

Acknowledgements

The author thanks M. Rypdal for many stimulating discussions, L. Jackson and V. Skiba for helpful comments and A. Robinson for providing the time series of the AMOC strength and SST-based AMOC index from the different CMIP control simulations. N.B. acknowledges funding by the Volkswagen Foundation. This is TiPES contribution #116; the Tipping Points in the Earth System (TiPES) project has received funding from the European Union's Horizon 2020 research and innovation programme under grant agreement no. 820970.

Competing interests

The author declares no competing interests.

Additional information

Extended data is available for this paper at https://doi.org/10.1038/s41558-021-01097-4.

Supplementary information The online version contains supplementary material available at https://doi.org/10.1038/s41558-021-01097-4.

Correspondence and requests for materials should be addressed to N.B.

Peer review information *Nature Climate Change* thanks Matthias Prange and the other, anonymous, reviewer(s) for their contribution to the peer review of this work.

Reprints and permissions information is available at www.nature.com/reprints.

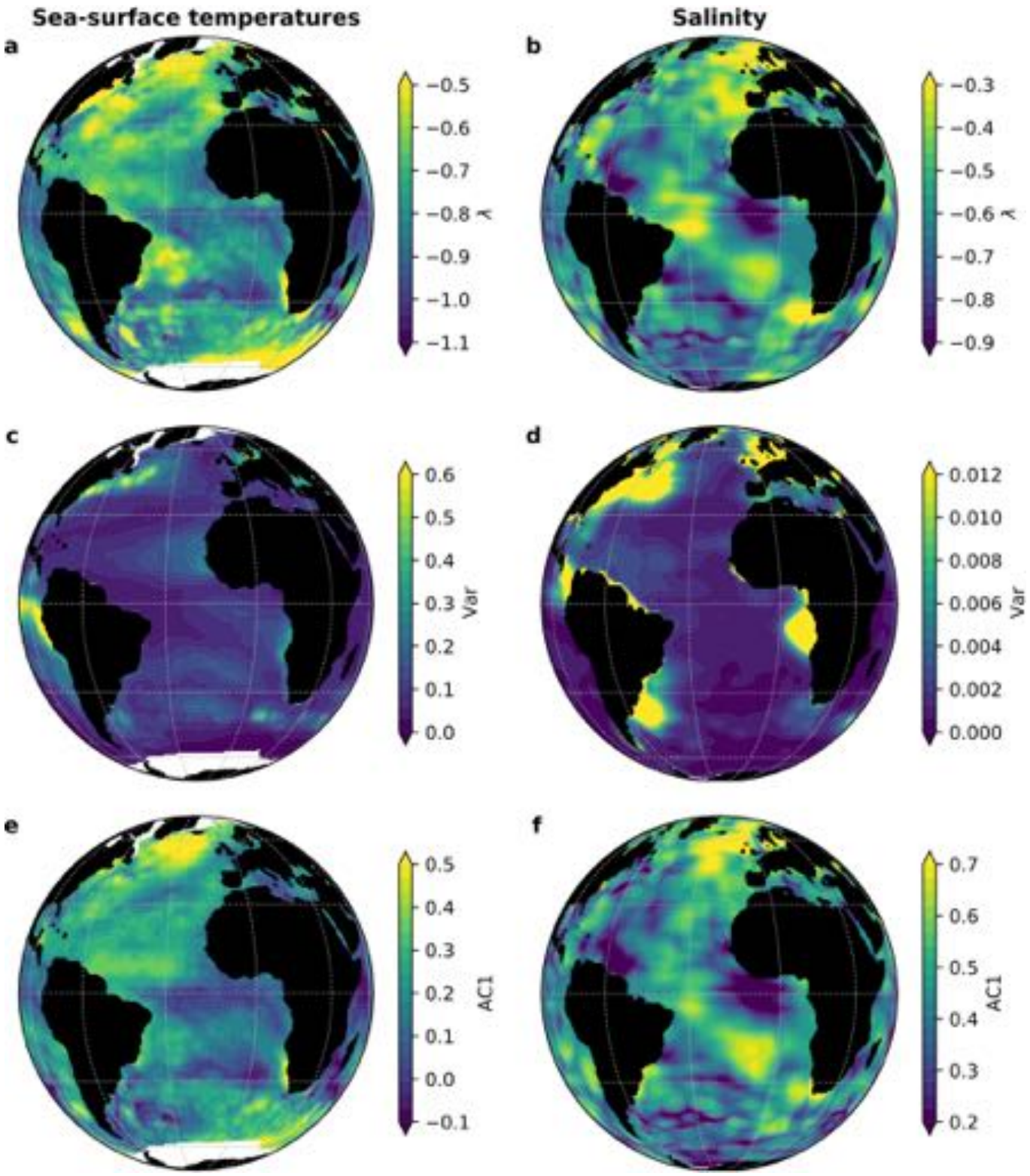

Extended Data Fig. 1 | Mean early-warning indicators for the Atlantic ocean. a, Corrected restoring rate λ estimated from the HadISST dataset assuming autocorrelated noise. **b**, Same as (a) but for the EN4 salinity dataset. **c**, Variance estimated from the HadISST dataset. **d**, Same as (c) but for the EN4 salinity dataset. **e**, AC1 estimated from the HadISST dataset. **f**, Same as (e) but for the EN4 salinity dataset. Note the high values in the northern Atlantic and the subpolar gyre region in particular for λ and AC1.

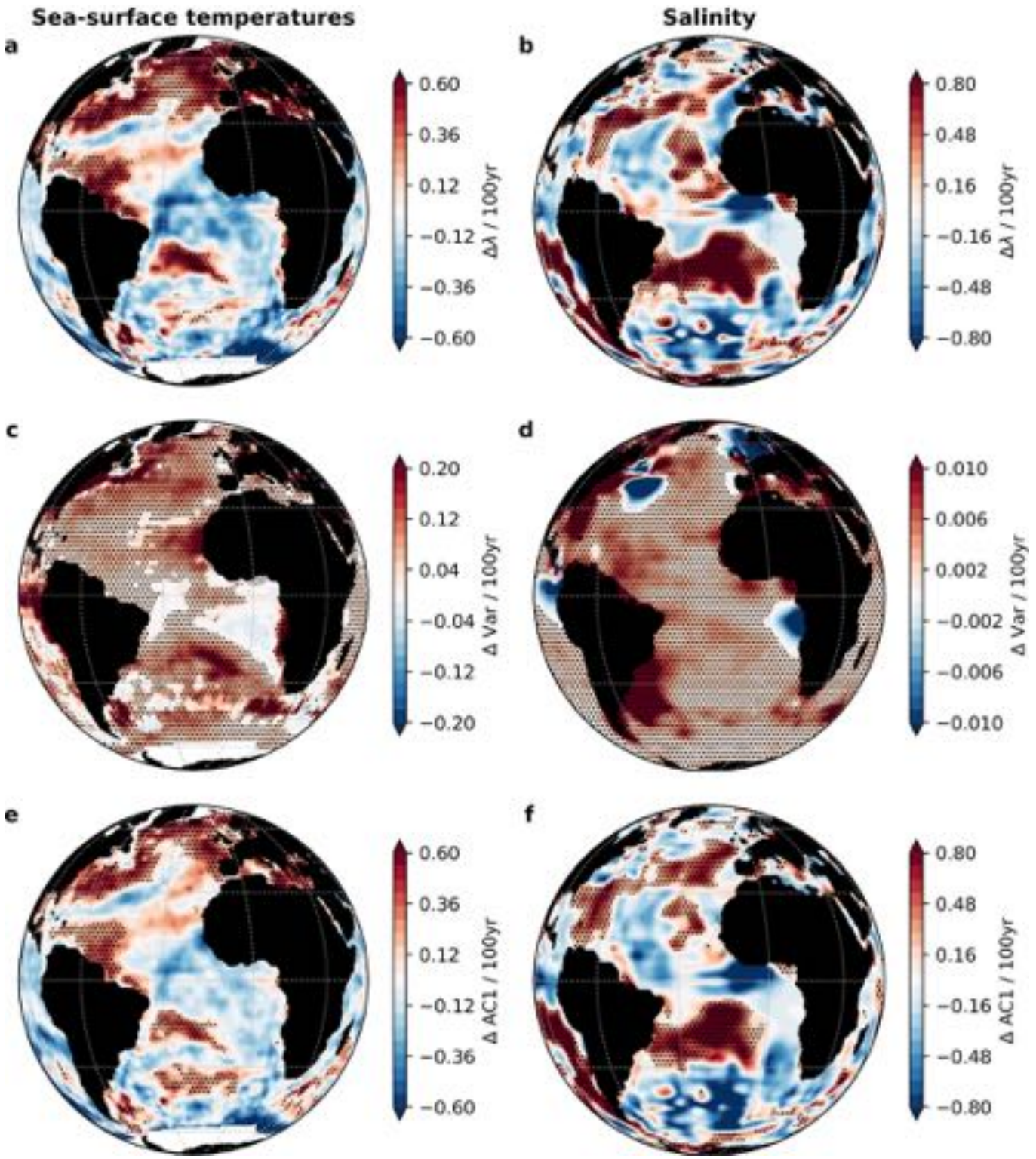

Extended Data Fig. 2 | Trends of early-warning indicators for the Atlantic ocean. a, Linear trends of the corrected restoring rate λ estimated from the HadISST dataset assuming autocorrelated noise. **b**, Same as (a) but for the EN4 salinity dataset. **c**, Linear trends of the variance estimated from the HadISST dataset. **d**, Same as (c) but for the EN4 salinity dataset. **e**, Linear trends of the AC1 estimated from the HadISST dataset. **f**, Same as (e) but for the EN4 salinity dataset. Note the high positive values in the northern Atlantic and the subpolar gyre region in particular for λ and AC1, but also in the southern Atlantic ocean where a salinity pileup has recently been associated with an AMOC slowdown [46].

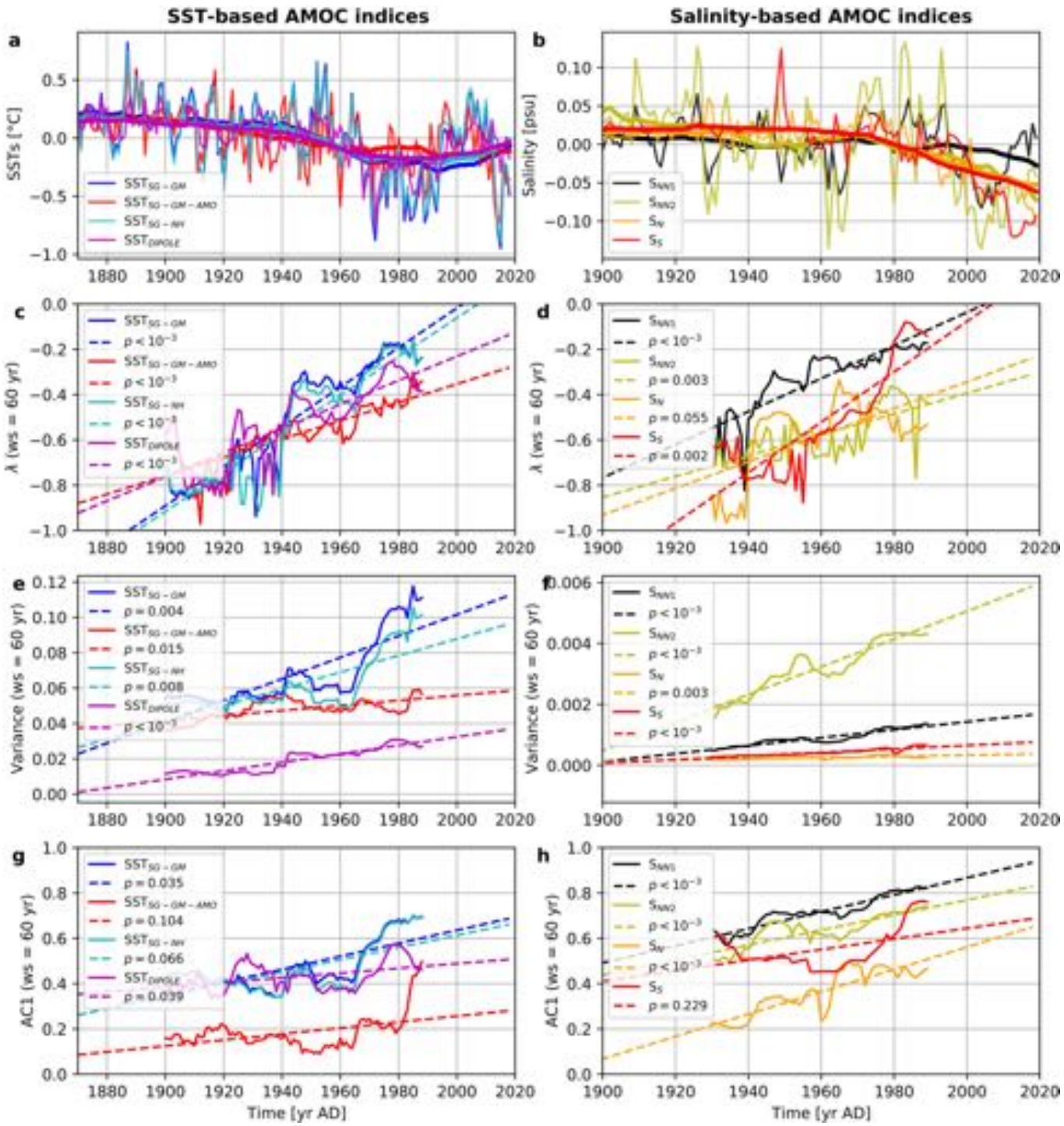

Extended Data Fig. 3 | Same as Fig. 3, but with sliding window size $w = 60$ yr to estimate EWS. a, SST-based AMOC indices (thin) together with 50-yr running means (thick). **b**, Salinity-based AMOC indices (thin) together with 50-yr running means (thick). **c**, The restoring rate λ of the SST-based AMOC indices, estimated under the assumption of autocorrelated noise. **d**, The restoring rate λ of the salinity-based AMOC indices, estimated under the assumption of autocorrelated noise. **e**, Same as (c) but for the variance. **f**, Same as (d) but for the variance. **g**, Same as (c) but for the AC1. **h**, Same as (d) but for the AC1. The dashed lines indicate the linear trends of the three early-warning indicators, with p-values given in the legends. Values for each sliding window are plotted at the centre point of that window. Data for the first and the last $w/2 = 30$ yr are omitted because no full time windows to estimate the different early-warning indicators are available there.

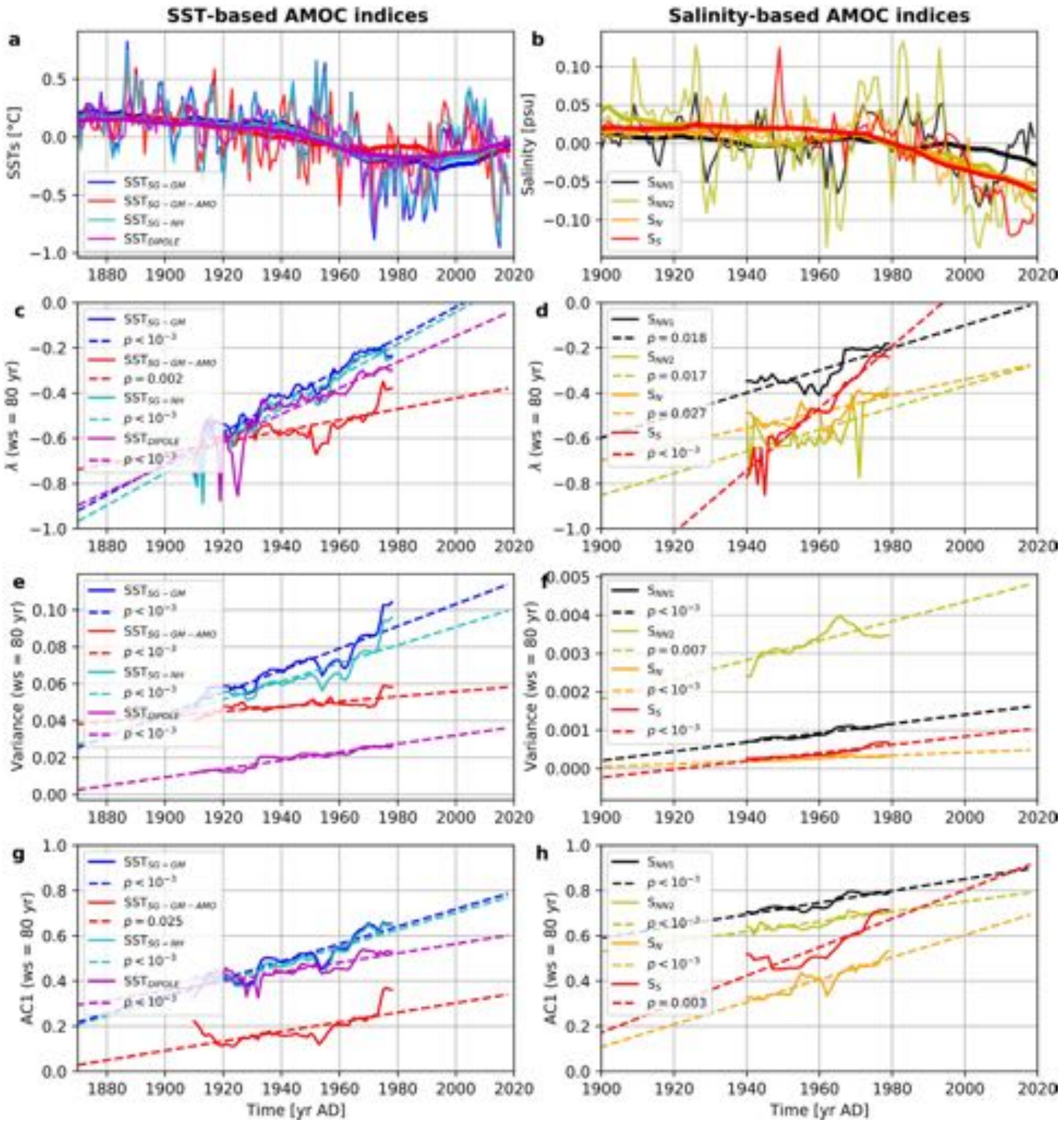

Extended Data Fig. 4 | Same as Fig. 3, but with sliding window size $w = 80$ yr to estimate EWS. a, SST-based AMOC indices (thin) together with 50-yr running means (thick). **b**, Salinity-based AMOC indices (thin) together with 50-yr running means (thick). **c**, The restoring rate λ of the SST-based AMOC indices, estimated under the assumption of autocorrelated noise. **d**, The restoring rate λ of the salinity-based AMOC indices, estimated under the assumption of autocorrelated noise. **e**, Same as (c) but for the variance. **f**, Same as (d) but for the variance. **g**, Same as (c) but for the AC1. **h**, Same as (d) but for the AC1. The dashed lines indicate the linear trends of the three early-warning indicators, with *p*-values given in the legends. Values for each sliding window are plotted at the centre point of that window. Data for the first and the last $w/2 = 40$ yr are omitted because no full time windows to estimate the different early-warning indicators are available there.

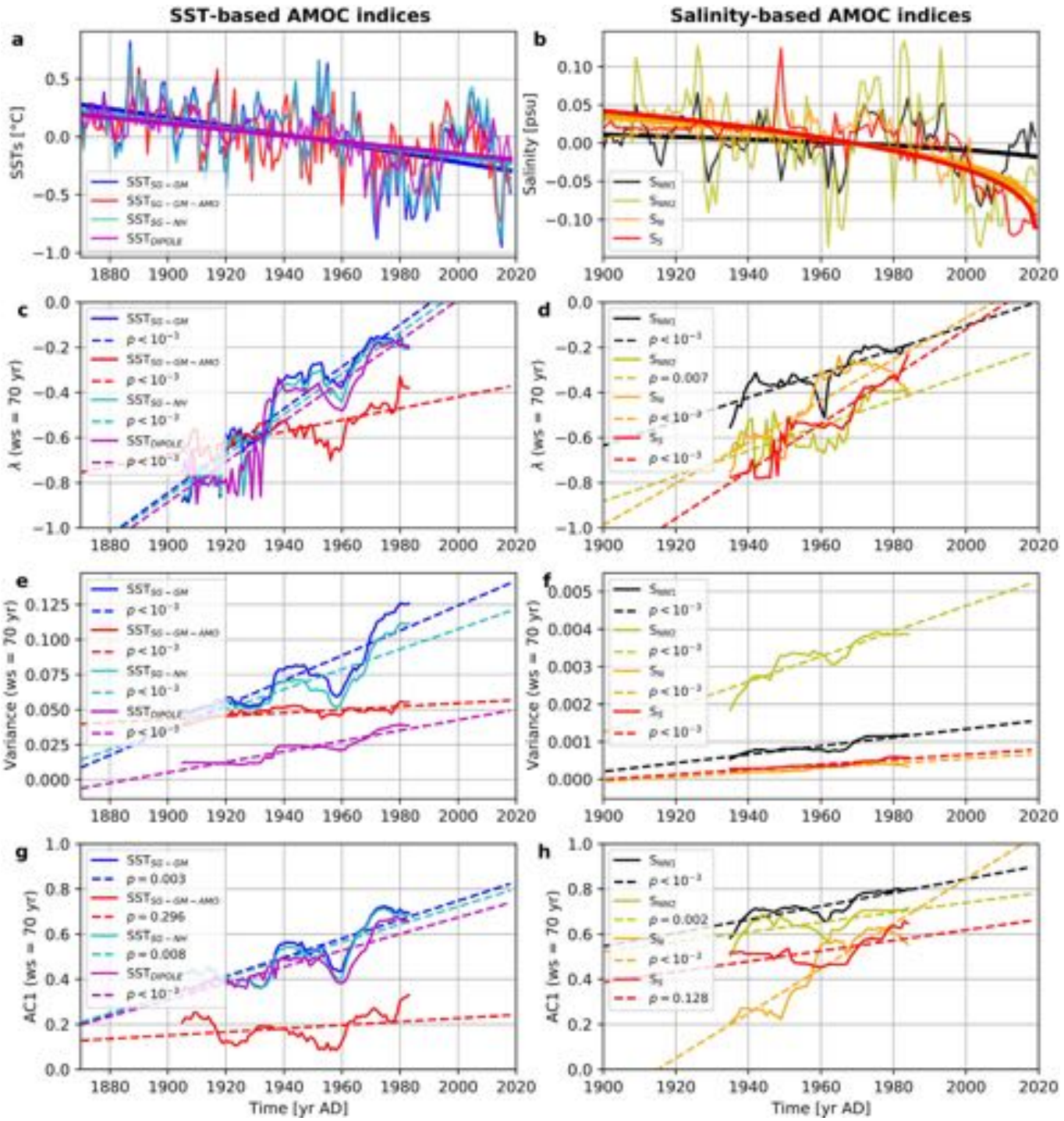

Extended Data Fig. 5 | Same as Fig. 4 in the main text, but for the remaining six AMOC indices as indicated in the legends. a, SST-based AMOC indices and fitted fixed point of a conceptual AMOC model. **b**, Salinity-based AMOC indices and fitted fixed point of a conceptual AMOC model. **b**,**c**, The restoring rate λ of the SST-based AMOC indices, estimated under the assumption of autocorrelated noise. **d**, The restoring rate λ of the salinity-based AMOC indices, estimated under the assumption of autocorrelated noise. **e**, Same as (c) but for the variance. **f**, Same as (d) but for the variance. **g**, Same as (c) but for the AC1. **h**, Same as (d) but for the AC1. The dashed lines indicate the linear trends of the three early-warning indicators, with *p*-values given in the legends. Values for each sliding window are plotted at the centre point of that window. Data for the first and the last $w/2 = 35$ yr are omitted because no full time windows to estimate the different early-warning indicators are available there.

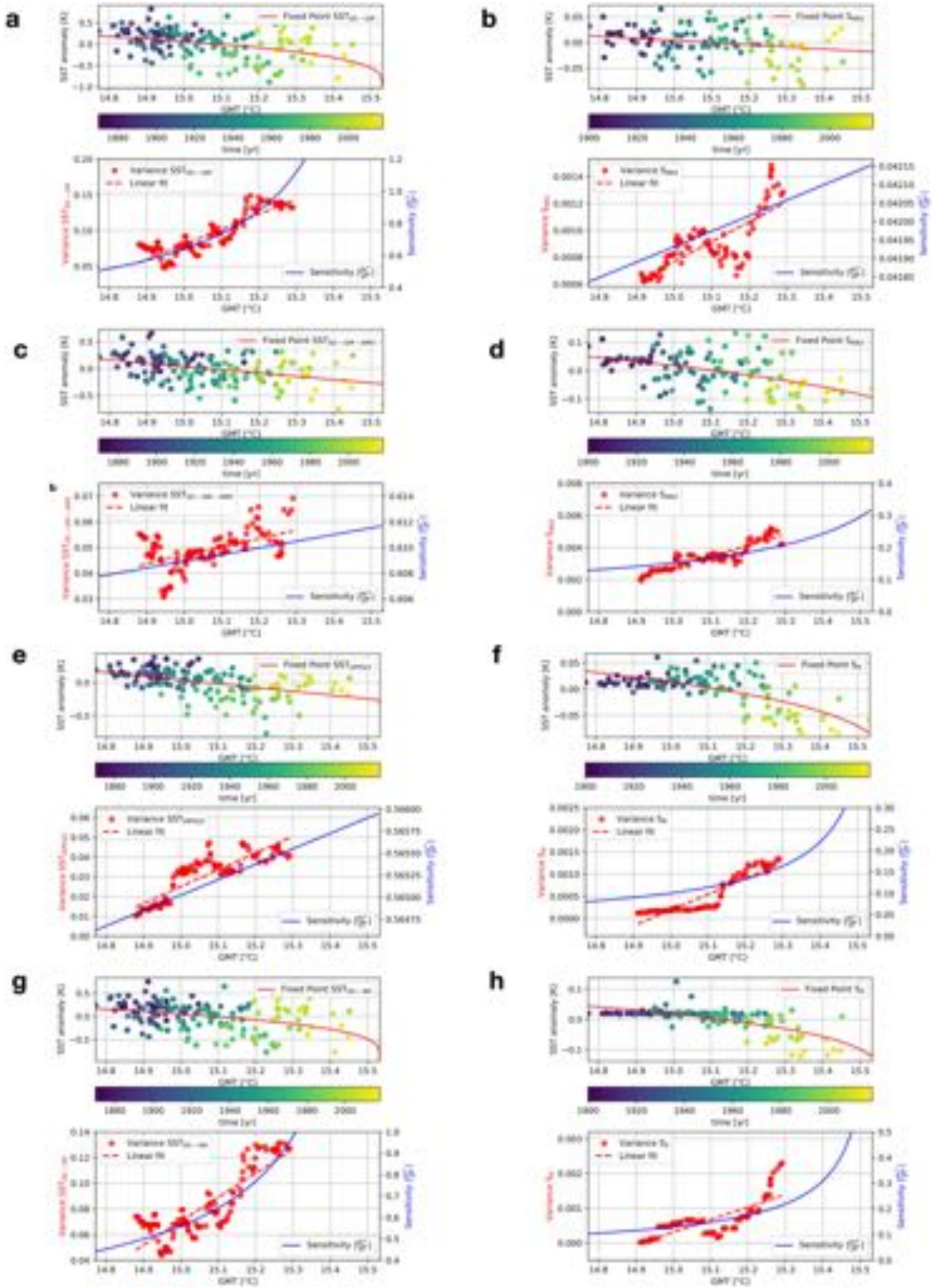

Extended Data Fig. 6 | Same as Fig. 5 in the main text, but for all eight AMOC indices SST_{SG-GM} (a), $SST_{SG-GM-AMO}$ (c), $SST_{DIPOOLE}$ (e), SST_{SG-NH} (g), S_{NN1} (b), S_{NN2} (d), S_N (f), and S_S (h) as indicated in the legends. In each panel, the respective AMOC index (top) and the corresponding variance (bottom) are shown as functions of the control parameter *T*.

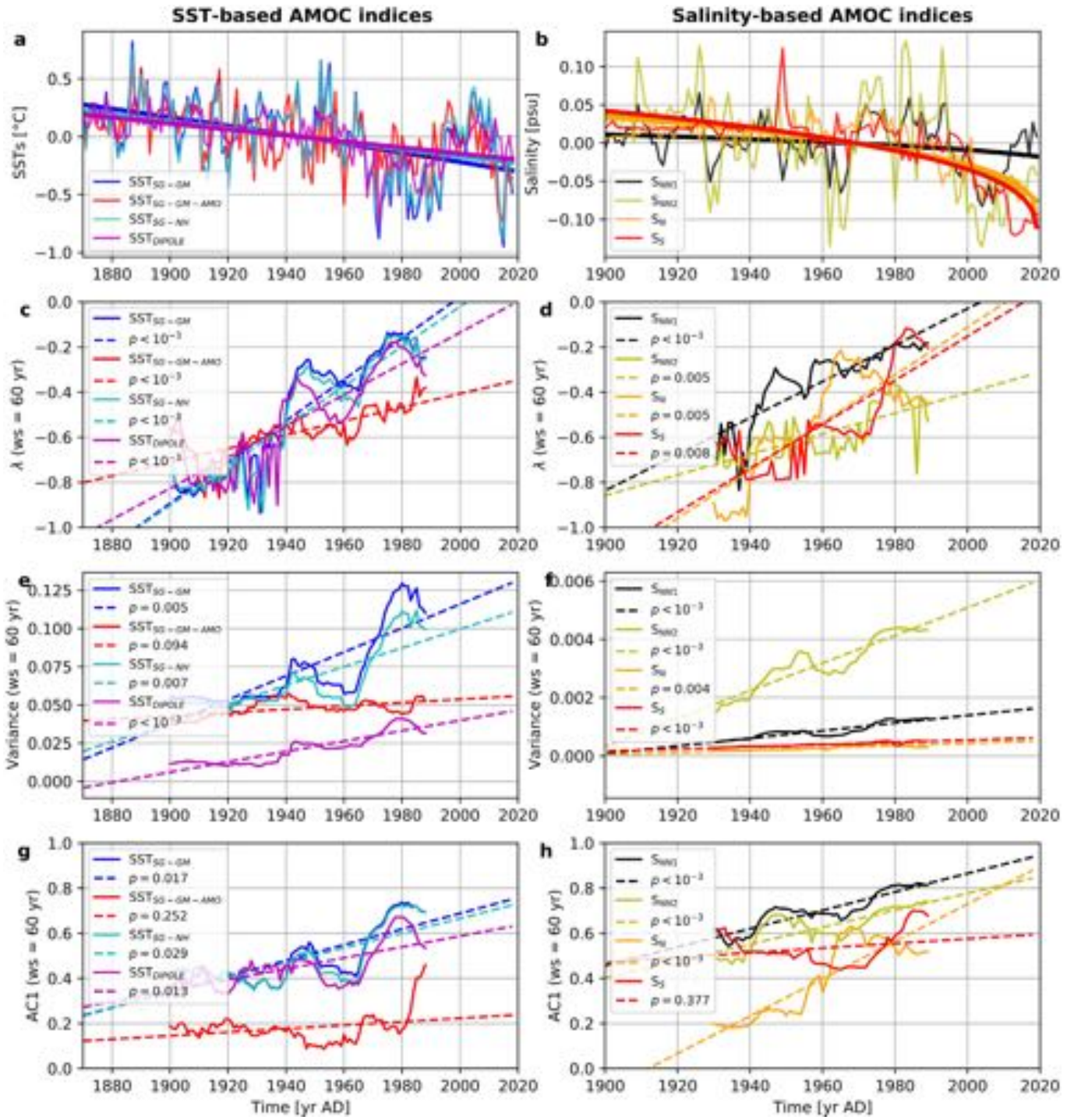

Extended Data Fig. 7 | Same as Extended Data Fig. 5, but with sliding window size $w = 60$ yr to estimate EWS. a, SST-based AMOC indices and fitted fixed point of a conceptual AMOC model. **b**, Salinity-based AMOC indices and fitted fixed point of a conceptual AMOC model. **b**,**c**, The restoring rate λ of the SST-based AMOC indices, estimated under the assumption of autocorrelated noise. **d**, The restoring rate λ of the salinity-based AMOC indices, estimated under the assumption of autocorrelated noise. **e**, Same as (c) but for the variance. **f**, Same as (d) but for the variance. **g**, Same as (c) but for the AC1. **h**, Same as (d) but for the AC1. The dashed lines indicate the linear trends of the three early-warning indicators, with p-values given in the legends. Values for each sliding window are plotted at the centre point of that window. Data for the first and the last $w/2 = 30$ yr are omitted because no full time windows to estimate the different early-warning indicators are available there.

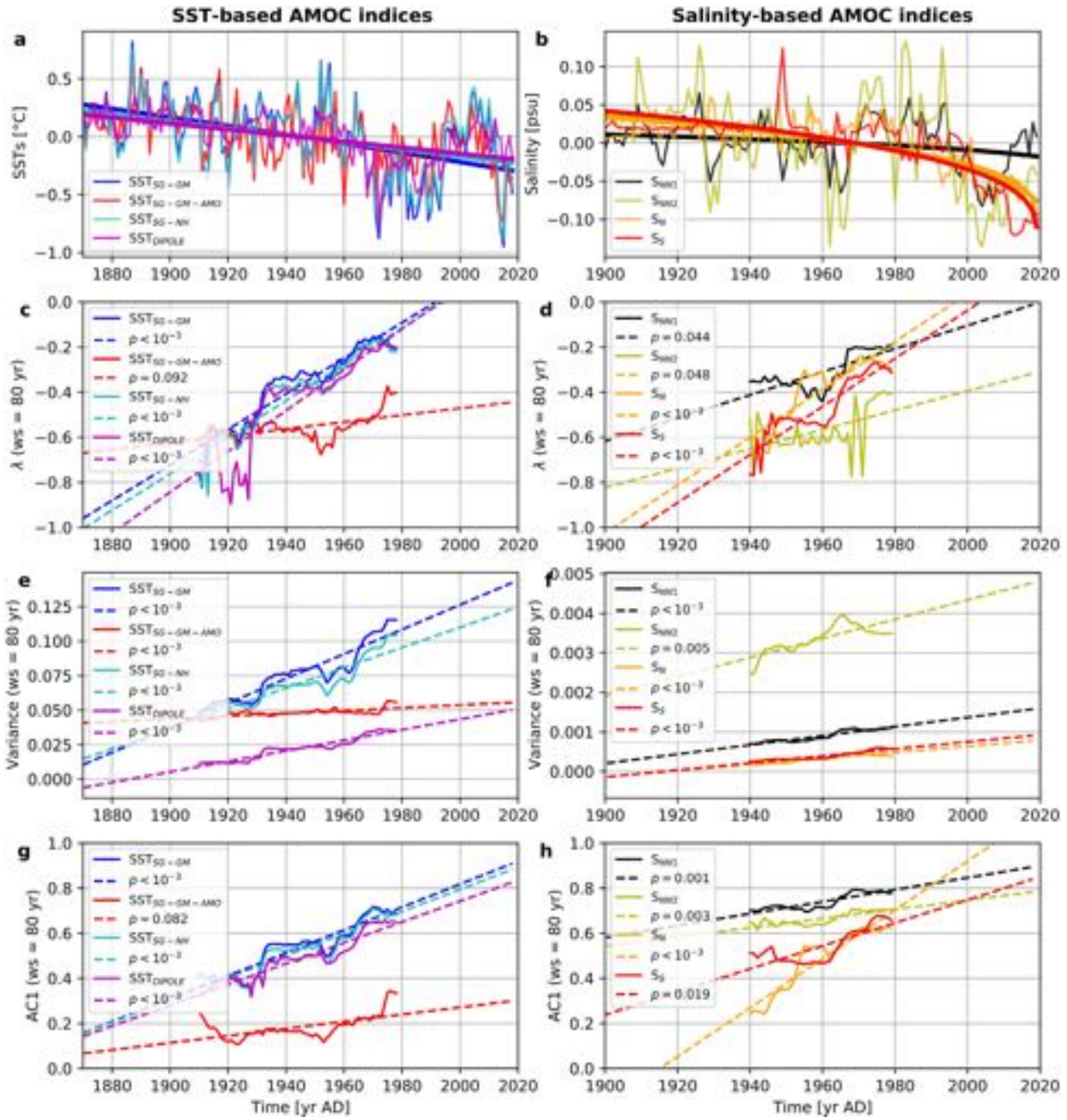

Extended Data Fig. 8 | Same as Extended Data Fig. 5, but with sliding window size $w = 80$ yr to estimate EWS. a, SST-based AMOC indices and fitted fixed point of a conceptual AMOC model. **b**, Salinity-based AMOC indices and fitted fixed point of a conceptual AMOC model. **b**,**c**, The restoring rate λ of the SST-based AMOC indices, estimated under the assumption of autocorrelated noise. **d**, The restoring rate λ of the salinity-based AMOC indices, estimated under the assumption of autocorrelated noise. **e**, Same as (c) but for the variance. **f**, Same as (d) but for the variance. **g**, Same as (c) but for the AC1. **h**, Same as (d) but for the AC1. The dashed lines indicate the linear trends of the three early-warning indicators, with p-values given in the legends. Values for each sliding window are plotted at the centre point of that window. Data for the first and the last $w/2 = 40$ yr are omitted because no full time windows to estimate the different early-warning indicators are available there.

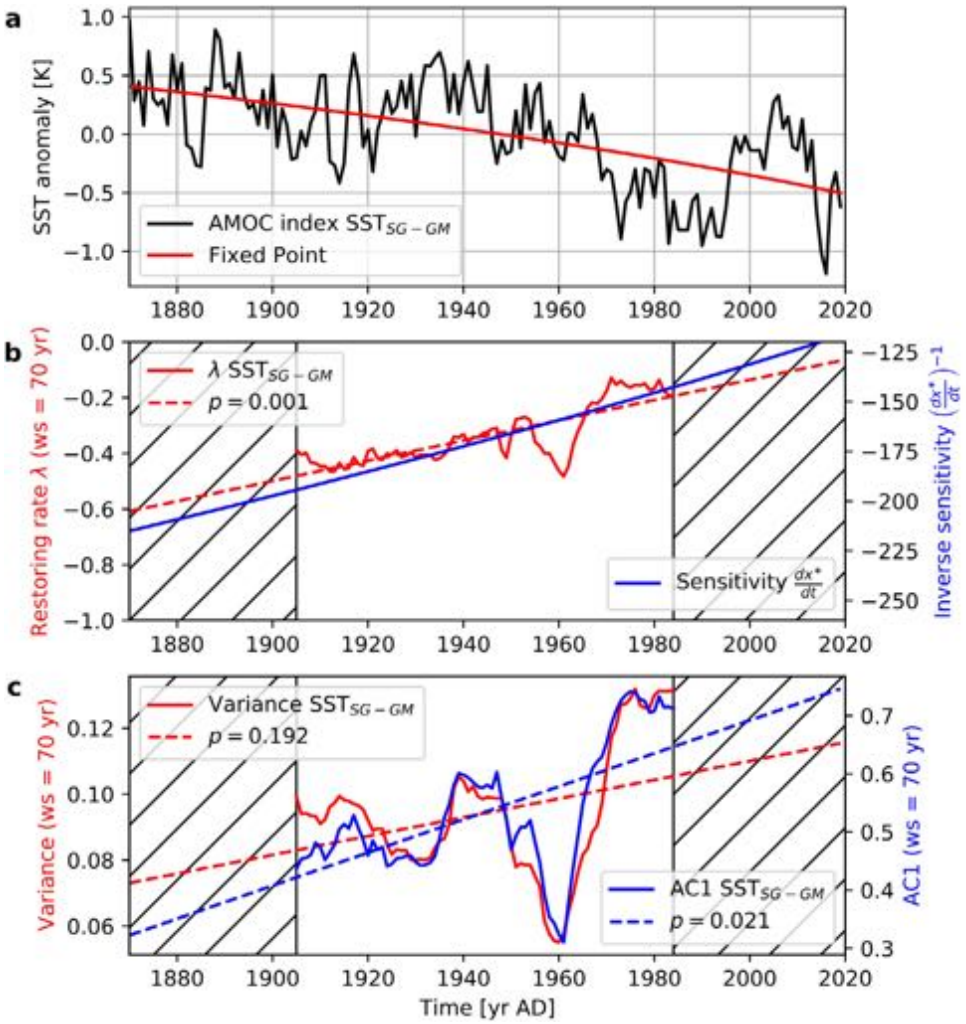

Extended Data Fig. 9 | Early-warning signals for the SST-based AMOC index SST_{SG-GM}. Same as Fig. 4, but using the ERSST instead of the HadISST dataset.

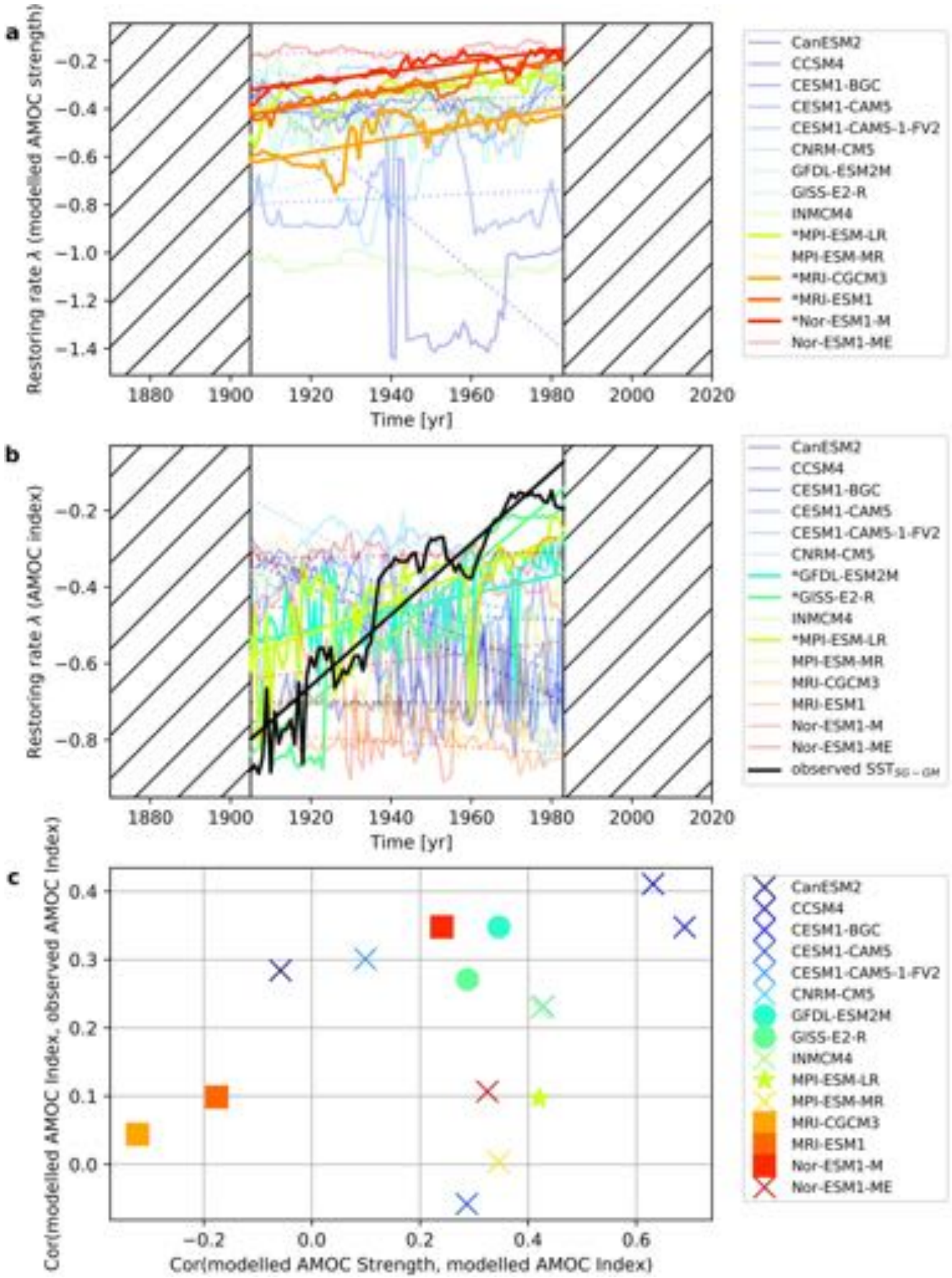

Extended Data Fig. 10 | AMOC strength and SST-based index in CMIP5 models. Same as Fig. 6, but for the modelled maximum AMOC strength over all ocean depths from 20°N to 60°N, instead of at 26°N.